Dual energy CT for more accurate diagnosis and monitoring of early osteoarthritis-related shoulder injuries

by

Sarah Quayyum

A thesis
presented to the University of Waterloo
in fulfillment of the
thesis requirement for the degree of
Master of Science
in
Kinesiology and Health Sciences

Waterloo, Ontario, Canada, 2025

© Sarah Quayyum 2025

Author's Declaration

I hereby declare that I am the sole author of this thesis document. This is a true copy of the thesis, including any required final revisions, as accepted by my examiners.

I understand that my thesis may be made electronically available to the public.

Abstract

The rapid acceleration of population aging has led to a growing prevalence of age-related musculoskeletal (MSK) conditions, such as osteoarthritis (OA). Dual-energy CT (DECT) is an advanced imaging modality that shows promise in enhancing the diagnosis and characterization of MSK disorders by providing improved visualization of joint and tissue changes after injury. These advancements may support more effective treatment planning and better patient outcomes. The primary aim of this study was to refine input parameters used in DECT imaging and apply them to better understand the relationship between shoulder injury and early osteoarthritic changes over a six month period. This knowledge is expected to improve therapeutic outcomes and support early screening for individuals at high risk of developing OA. DECT was employed to quantify volumetric bone mineral density (vBMD) and to model bone stiffness and loading using Finite Element Modeling (FEM) in both cadaveric specimens and participants. Three anatomical regions of the proximal humerus were assessed: the humeral shaft diaphysis, the articular surface of the humerus (humeral head), and the anatomical neck. Cadaveric scans were performed using both dipotassium phosphate (K_2HPO_4) and hydroxyapatite (HA) calibration phantoms while participants were scanned using only the HA phantom. Imaging was conducted using both BONE and Standard (STD) reconstruction kernels at three energy pair combinations: 40/90, 90/140, and 40/140 keV. These combinations were chosen to evaluate whether higher energy pairs could help mitigate attenuation issues commonly encountered at lower energy pair combinations. The BONE kernel was selected for its superior bone edge sharpening and contrast, whereas the STD kernel was used to enhance visualization of surrounding soft tissues. Participant imaging occurred at baseline (within six weeks of injury) and again at six-month follow-up. Results of this study demonstrated that both vBMD and FEM stiffness values were significantly higher in the diaphysis when scanned using the BONE kernel at the highest energy pair combination (90/140 keV). In contrast, the anatomical neck consistently showed the lowest vBMD and stiffness values, with no significant differences in vBMD or FEM values observed within the anatomical neck or humeral head regions under the same parameters. By developing patient-specific, image-based computational models, this study contributes to a deeper understanding of both biomechanical and imaging characteristics of early shoulder OA, potentially informing future diagnostic and therapeutic strategies.

Acknowledgements

I would like to express my deepest gratitude to my defense committee, Dr. Monica Maly and Dr. Clark Dickerson, for their invaluable feedback. I also could not have undertaken this journey without my supervisor, Dr. Nikolas Knowles, who generously provided his knowledge and expertise in the field of medical imaging. Additionally, this endeavor would not have been possible without the generous support from the Arthritis Society Canada.

Dedication

To my family and friends— thank you for being my constant. This thesis exists because you reminded me I could do hard things, even when I didn't believe it myself. To my mom - through every late night, every meltdown, and every moment of doubt, you were there. Your words, your hugs, your check-ins, your quiet belief in me—it all meant more than I can ever express. I hope this makes you proud, because I couldn't have done it without you.

Table of Contents

Author's Declaration ii

Abstract iii

Acknowledgements iv

Dedication v

List of Figures ix

List of Tables xi

List of Abbreviations xiv

1 Introduction 1

1.1 Background 1

1.2 Shoulder anatomy 2

1.3 Prevalence and importance of shoulder OA 3

1.3.1 Negative impact on the quality of life 4

1.3.2 Economic and healthcare costs 4

1.3.3 Burden on individuals and society 5

1.3.4 Gaps in literature and research 5

1.4 Risk factors for shoulder OA . . . 6
1.4.1 Dislocations and subluxations . . . 6
1.4.2 Bone morphology and shape . . . 7
1.4.3 Bone sclerosis . . . 7
1.5 Overview of dual-energy CT technology . . . 8
1.5.1 Simulated monochromatic images . . . 9
1.5.2 Density calibration phantoms . . . 10
1.5.3 Bone sharpening (BONE) and standard smoothing (STD) reconstruction kernels . . . 12
1.5.4 Volumetric bone mineral density . . . 14
1.5.5 Bone marrow lesions . . . 15
1.5.6 Finite element modeling . . . 17
1.6 Clinical applications in MSK assessment . . . 18
1.7 Diagnostic performance and accuracy of DECT in identifying MSK injuries 19
1.8 Comparative analysis of DECT with other imaging methods . . . 19
1.9 Cost effectiveness of DECT . . . 20
1.10 Challenges and limitations in the use of DECT . . . 21
1.11 Research objectives and aims . . . 22
1.12 Hypothesis . . . 25

2 Methodology **26**
2.1 Participants . . . 26
2.2 Medical imaging . . . 27
2.3 Image processing and volumetric bone mineral density (vBMD) analysis . . . 28
2.3.1 Finite element model (FEM) generation . . . 31
2.4 Statistical analysis . . . 31

3 Results **33**

3.1 Cadaver specimens vBMD results 33

3.2 Participants vBMD results 37

3.3 Participants follow-up vBMD results 38

3.4 Cadaver specimens FEM results 39

3.5 Participants baseline FEM results 41

3.6 Participants follow-up FEM results 42

3.7 Regression parameters for vBMD vs. Stiffness 43

3.8 K_2HPO_4 vs. HA Regression Plots 43

4 Discussion **46**

4.1 Limitations 48

4.2 Conclusion 49

References **51**

APPENDIX **62**

A Mathematical equations for CT image analysis **63**

A.1 Volumetric bone mineral density (vBMD) calibration method 63

List of Figures

1.1 Anatomy of glenohumeral joint [37]. 3

1.2 Comparison of the spectra of monochromatic and polychromatic X-ray beams [67]. 11

1.3 An example of a density calibration phantom [57]. 12

1.4 Representative axial DECT images of an isolated cadaveric shoulder generated using two reconstruction kernels (BONE and STD). 14

1.5 MRI scans identifying the Costa-Paz et al [22] subchondral TBML classifications in the knee; (A) type I lesion, diffuse signal with change of medullary component, can be reticular and distant from subjacent articular surface; (B) type II lesion, localized signal with contiguity to the subjacent articular surface, often crescentic in shape; (C) type III lesion, disruption of the normal contour of the cortical surface, often associated with type II lesions [74]. 16

1.6 DECT scans overlaying sections of the proximal humerus that were analyzed. 23

1.7 Flowchart displaying order of steps taken in the study, along with the relevant statistical measurements. 24

2.1 Stages of volumetric bone mineral density analysis and input to image-based finite element models for the study. 30

2.2 Stages of finite element model analysis for the study. 31

3.1 Linear regression of K_2HPO_4 vs. HA within each kernel and energy pair combination in the humeral shaft diaphysis. 44

3.2 Linear regression of K_2HPO_4 vs. HA within each kernel and energy pair combination in the anatomical neck. 44

3.3 Linear regression of K_2HPO_4 vs. HA within each kernel and energy pair combination in the humeral head. 45

List of Tables

1.1 Definition of the types of traumatic bone marrow lesions based on the Costa-Paz classification system [22, 74]. 17

2.1 Demographic characteristics and sectioning of cadaver specimens being scanned for study. 26

3.1 Volumetric bone mineral density (vBMD) in the **humeral shaft diaphysis of cadaver specimens** derived using two dual-energy CT reconstruction kernels with three energy pair combinations using the $\boldsymbol{K_2HPO_4}$ calibration phantom. 34

3.2 Volumetric bone mineral density (vBMD) in the **humeral shaft diaphysis of cadaver specimens** derived using two dual-energy CT reconstruction kernels with three energy pair combinations using the **HA** calibration phantom. 35

3.3 Volumetric bone mineral density (vBMD) in the **anatomical neck of the humerus of cadaver specimens** derived using two dual-energy CT reconstruction kernels with three energy pair combinations using the **HA** calibration phantom. 35

3.4 Volumetric bone mineral density (vBMD) in the **anatomical neck of the humerus of cadaver specimens** derived using two dual-energy CT reconstruction kernels with three energy pair combinations using the $\boldsymbol{K_2HPO_4}$ calibration phantom. 36

3.5 Volumetric bone mineral density (vBMD) in the **articular surface of the humerus head of cadaver specimens** derived using two dual-energy CT reconstruction kernels with three energy pair combinations using the **HA** calibration phantom. 36

3.6 Volumetric bone mineral density (vBMD) in the **articular surface of the humerus head of cadaver specimens** derived using two dual-energy CT reconstruction kernels with three energy pair combinations using the K_2HPO_4 calibration phantom. 37

3.7 Volumetric bone mineral density (vBMD) in the **humeral shaft diaphysis of participants** derived using two dual-energy CT reconstruction kernels with three energy pair combinations using the **HA** calibration phantom. . 37

3.8 Volumetric bone mineral density (vBMD) in the **anatomical neck of the humerus of participants** derived using two dual-energy CT reconstruction kernels with three energy pair combinations using the **HA** calibration phantom. 38

3.9 Volumetric bone mineral density (vBMD) in the **articular surface of the humerus head of participants** derived using two dual-energy CT reconstruction kernels with three energy pair combinations using the **HA** calibration phantom. 38

3.10 Volumetric bone mineral density (vBMD) at **6-month follow-up** in the **humeral shaft diaphysis of participants** derived using two dual-energy CT reconstruction kernels with three energy pair combinations using the **HA** calibration phantom. 39

3.11 Volumetric bone mineral density (vBMD) at **6-month follow-up** in the **anatomical neck of the humerus of participants** derived using two dual-energy CT reconstruction kernels with three energy pair combinations using the **HA** calibration phantom. 39

3.12 Volumetric bone mineral density (vBMD) at **6-month follow-up** in the **articular surface of the humerus head of participants** derived using two dual-energy CT reconstruction kernels with three energy pair combinations using the **HA** calibration phantom. 39

3.13 Finite element modeled (FEM) stiffness in the **humeral shaft diaphysis of cadaver specimens** derived using two dual-energy CT reconstruction kernels with three energy combinations using the K_2HPO_4 calibration phantom. 40

3.14 Finite element modeled (FEM) stiffness in the **anatomical neck of the humerus of cadaver specimens** derived using two dual-energy CT reconstruction kernels with three energy combinations using the K_2HPO_4 calibration phantom. 41

3.15 Finite element modeled (FEM) stiffness in the **humeral shaft diaphysis of participants** derived using two dual-energy CT reconstruction kernels with three energy combinations using the **HA** calibration phantom. 41

3.16 Finite element modeled (FEM) stiffness in the **anatomical neck of the humerus of participants** derived using two dual-energy CT reconstruction kernels with three energy combinations using the **HA** calibration phantom. 42

3.17 Finite element modeled (FEM) stiffness at **six-months follow-up** in the **humeral shaft diaphysis of participants** derived using two dual-energy CT reconstruction kernels with three energy combinations using the **HA** calibration phantom. 42

3.18 Finite element modeled (FEM) stiffness at **six-months follow-up** in the **anatomical neck of the humerus of participants** derived using two dual-energy CT reconstruction kernels with three energy combinations using the **HA** calibration phantom. 42

3.19 Regression parameters for vBMD and FEM-based stiffness from the proximal humerus models in cadaver specimens from two dual-energy CT reconstruction kernels with three energy combinations. 43

List of Abbreviations

K_2HPO_4 liquid dipotassium phosphate 27, 28, 31, 63

BMLs bone marrow lesions 9, 15, 18, 19, 21, 22, 49

DECT Dual-energy CT iii, 2, 8, 9, 12–23, 26–29, 32, 43, 46–49, 63

FEM Finite Element Modeling iii, 17, 22, 23, 28, 29, 33, 39–43, 46–49

FOV field of view 22, 27

HA hydroxyapatite 27–29, 31, 63

MSK Musculoskeletal 1, 2, 18–20

OA osteoarthritis iii, 1, 3–8, 10, 15, 17, 22, 46–50

PACS picture archiving and communication system 21

SECT single-energy CT 21, 22

TBMLs Traumatic bone marrow lesions 15, 16

vBMD volumetric bone mineral density iii, 14, 15, 17, 22, 28, 29, 31–34, 37, 38, 43, 46–49, 63

VMI virtual monochromatic images 9

VNCa Virtual non-calcium 8, 9, 21

Chapter 1

Introduction

1.1 Background

Population aging is accelerating at unprecedented rates [11]. Musculoskeletal (MSK) disorders and injuries are common conditions that can significantly impact an individual's quality of life [11]. As the population continues to age, the prevalence of age-related MSK conditions—such as OA, fractures, and sprains—is expected to rise, increasing the demand for healthcare interventions and services.

Shoulder OA is a gradual, progressive, mechanical and biochemical breakdown of the articular cartilage and other joint tissues, including the bone and joint capsule of the shoulder [19]. As the articular surfaces of the humeral head and glenoid wears, friction within the joint increases, causing progressive loss of the normal load-bearing surfaces, leading to pain and disability [55]. There are multiple risk factors for developing shoulder OA, including age, genetics, sex, weight, joint infection, history of shoulder dislocation, and previous injury, and certain heavy occupations or overhead sports [55]. Although not as commonly prevalent as OA in other locations, such as in the knee and hips, shoulder OA can be just as debilitating due to the functional importance of the upper limbs [39]. Pain and functional impairment can affect the physical as well as the psychological well-being, causing limitations in occupational and leisure activities in younger individuals and threatening the physical independence in elderly populations [39]. Shoulder OA can be divided into primary and secondary categories: primary OA is more prevalent, with no specific cause or predisposing factors that could lead to joint malfunction, while secondary OA typically has a known cause or predisposing factor, such as major shoulder trauma, recurrent instability and dislocations, infection, congenital malformations, or chronic rotator cuff tears [19].

The introduction of advanced imaging techniques, such as magnetic resonance imaging (MRI), multi-detector computed tomography (CT), dual-energy CT (DECT), and positron emission tomography (PET), has significantly enhanced the detection and characterization of MSK disorders [73]. These technologies provide physicians with valuable tools for accurate diagnosis and assessment, enabling more effective treatment planning and improved patient outcomes [73]. However, conventional CT and MRI have several limitations in precisely identifying and characterizing MSK injuries and disorders. Improvements in advanced quantitative imaging techniques, such as DECT, have shown promising results in improving our knowledge of MSK disorders and countering the limitations posed by MRI and conventional CT [89]. Recently, the technological innovation of fast KV-switching DECT, or dual-source DECT, has enabled the detection and characterization of bone abnormalities with high sensitivity and specificity [63]. DECT has shown promise in improving the diagnosis and characterization of musculoskeletal disorders by providing accurate material decomposition images and offering more precise quantification of tissue composition [73].

1.2 Shoulder anatomy

The glenohumeral joint is a synovial joint formed between the head of the humerus and the glenoid cavity of the scapula. The articular surfaces include the large, rounded head of the humerus and the smaller shallow glenoid cavity. This cavity is deepened by a fibrocartilaginous rim called the glenoid labrum, which attaches around its edge. At the top, the labrum blends with the tendon of the long head of the biceps brachii, which attaches to the supra-glenoid tubercle and runs through the joint cavity above the humeral head [37].

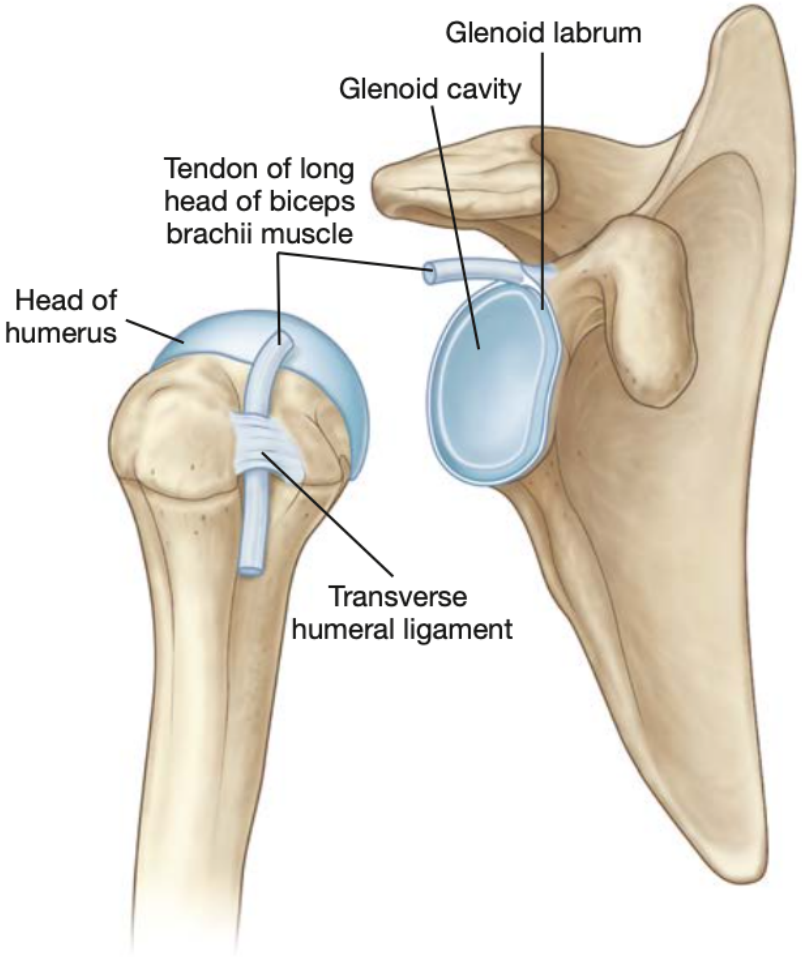


Figure 1.1: Anatomy of glenohumeral joint [37].

1.3 Prevalence and importance of shoulder OA

Shoulder OA, or OA in the glenohumeral joint, is less prevalent than OA in weight-bearing joints such as the hips and knees but still represents significant health issues for the aging population [3]. Although the exact prevalence of shoulder OA in Canada is not well-documented, a study conducted by the Arthritis Community Research and Evaluation Unit (ACREU) in 2010 estimated that around 5% of Canadians over the age of 50 experienced

symptomatic shoulder OA [3]. Approximately 3.9 million (13.6%) Canadians aged 20 years and older live with diagnosed osteoarthritis and 219,000 (8.7 per 1,000 persons per year) were newly diagnosed between 2016-2017 [61]. The prevalence and incidence of diagnosed OA generally increase with age and are higher among females (16.1% and 10.0 per 1,000 persons per year, respectively) compared to males (11.1% and 7.5 per 1,000 persons per year, respectively) [61]. In a study conducted in British Columbia, 18.4% of adults reported having OA, with prevalence ranging from 2.7% to 8.8% depending on the joint affected [48] Given these figures, it is reasonable to assume that shoulder OA affects a significant portion of the Canadian population, albeit less than OA in the knees or hips.

1.3.1 Negative impact on the quality of life

Shoulder OA can severely impact the quality of life of affected individuals due to severe pain, joint stiffness, and reduced mobility in the glenohumeral joint [3]. Unlike OA in weight-bearing joints, such as the hip or knee, shoulder OA primarily affects the ability of individuals to use the upper extremities. This can impair their capacity to perform activities of daily living including dressing, reaching, lifting, and significantly reduces functional independence, especially in the case of affected older adults [3]. The psychosocial consequences of shoulder OA are also a significant factor to consider. Chronic pain and disability from shoulder OA can lead to social isolation as individuals withdraw from activities they once enjoyed and contributed to, adding to their decline in mental health [3]. Anxiety and depression are common among those living with chronic pain conditions, further exacerbating the overall impact on their quality of life [3]. The mental health impact can be particularly severe in older adults where shoulder OA may limit their ability to maintain social connections, engage in hobbies, or stay active within their homes and communities [3].

1.3.2 Economic and healthcare costs

Managing shoulder OA can include frequent medical consultations, imaging studies, and ongoing physical therapy sessions. Pharmacological management for shoulder OA can often involve the long-term use of pain relievers, anti-inflammatory medications, and/or intra-articular injections which add to the cost [8]. For individuals living with severe OA, surgical interventions may sometimes be required (e.g., shoulder arthroplasty). These surgical interventions are costly and can require significant post-operative rehabilitation, adding to the overall financial burden on affected individuals [8]. In Canada, where healthcare

is publicly funded, the rising prevalence of shoulder OA, particularly among the aging population, can lead to increased healthcare expenditures [8]. As the population ages, the demand for shoulder-related healthcare services is expected to rise, potentially straining public healthcare resources [8]. Indirect costs also play a significant role including loss of productivity due to disability and the need for early retirement [8]. For individuals still in the workforce, shoulder OA can limit the ability to perform physically demanding tasks, leading to loss of work or the need to transition to less physically demanding roles that come with lower pay [8]. Furthermore, the need for long-term care, in cases where individuals can no longer care for themselves independently, can further increase the economic burden on societies and the healthcare systems [8].

1.3.3 Burden on individuals and society

The burden of shoulder OA extends beyond healthcare and economic costs. Individuals with shoulder OA often experience a decline in physical function of the upper extremities, resulting in needing assistance with activities of daily living either from family members or professional caregivers [3]. The reliance on others for basic tasks can lead to a loss of independence and dignity, further affecting the mental health and well-being of affected individuals, especially amongst older adults [3]. From a societal perspective, the cumulative effect of individuals living with shoulder OA contributes to a substantial loss of productivity [3]. This loss is particularly significant in occupations that require manual labor or repetitive upper-body movements where shoulder function is crucial [3]. Chronic pain associated with shoulder OA can also lead to mental health challenges, including depression and anxiety, which require additional healthcare resources for management [3, 8]. The societal cost of mental health conditions exacerbated by chronic pain, including the impact on families and communities, is considerable.

1.3.4 Gaps in literature and research

Shoulder OA is still an under-researched area compared to OA in other joints such as the hips and knees [3]. There is a lack of comprehensive epidemiological data on the prevalence and incidence of shoulder OA in not only Canada, but also globally [3, 61]. Currently, there are three main gaps in literature and research for shoulder OA: pathophysiology of shoulder OA, the effectiveness of treatments, and preventive measures [3]. While the pathophysiology of hip and knee OA is well-studied in literature and research, there is less understanding of how shoulder OA develops and progresses [3]. Moreover,

there is a need for more high-quality research studies to be conducted in order to evaluate the effectiveness of different treatment modalities for shoulder OA. Currently the research into preventive strategies for shoulder OA, including early intervention and lifestyle modifications, is limited.

1.4 Risk factors for shoulder OA

The risk of developing OA in individuals who have had a first-time traumatic shoulder dislocation is 10 to 20 times higher compared to the general population [20]. In a study by Kruckeberg et al., 2020 [50], approximately one in four patient under the age of 40 years with anterior shoulder instability developed symptomatic OA within 15 years of their first instability event (i.e., dislocations, subluxations, fractures). 55% of patients who sustained a first-time anterior shoulder dislocation before the age of 40 showed some degree of arthropathy on radiographs after 25 years, and in a preoperative analysis, 31% of patients with an anterior dislocation event before the age of 40 had arthritic changes visible on conventional CT scans [50].

1.4.1 Dislocations and subluxations

There is an increased risk of shoulder OA following shoulder dislocations and this risk is particularly significant if the dislocation causes damage to the cartilage, bones, or any other underlying structures within the shoulder joint [20]. Shoulder dislocations and subluxations can lead to OA of the glenohumeral joint through several mechanisms. During the dislocation or subluxation events, the articular cartilage surfaces can be damaged as the humeral head is forced out of the glenoid socket [20]. This damage may not fully heal, and repeated episodes can cause cumulative damage to the cartilage leading to degeneration over time, which is a key feature of OA [20]. Dislocations and subluxations of the shoulder joint can also stretch or tear the joint capsule, ligaments, and labrum, leading to joint laxity and instability and potentially accelerating cartilage wear [20]. Dislocations may also cause bony injuries such as Hill-Sachs lesions (a type of fracture that occurs secondary to an anterior shoulder dislocation) or glenoid bone loss, which can change the congruity of the joint and contact pressures [20]. Tears to the rotator cuff muscles during instability events can further destabilize the joint and contribute to OA development, and repeated instability episodes cause inflammation in the joint which over time can degrade the underlying cartilage and promote OA in the shoulder [20].

1.4.2 Bone morphology and shape

There is evidence suggesting that bone morphology changes can be used as a predictor to identify OA [5]. The relationship between bone shape and OA appears to be bi-directional, with shape abnormalities both contributing to and resulting from the disease process [5]. Studies have shown that the geometry of the hip joint is an important risk factor for OA, with subtle architectural changes predating the radiographic appearance of OA in the hips in up to 90% of cases presenting with abnormal hip joint morphology [5, 86]. Differences in hip joint geometry alters the distribution of loading forces across the weight-bearing joint. This can lead to problems such as a number of anatomic variants in the shape of the acetabular "cup" of the hip joint (acetabular dysplasia), femoro-acetabular impingement, non-spherical femoral head (pistol head) deformity, or wide femoral neck deformity [5]. Similarly, it has been appreciated for some time that malalignment of the knee is a predisposing factor for knee OA [5]. Abnormalities present in the shapes of the femur, tibia, patella, or a combination of all three have been identified as factors altering the distribution of forces across the knee joint, and as predisposing factors for OA in the knees [5, 86].

Glenohumeral OA causes progressive joint damage characterized by extensive bone remodeling and osteophyte formation [42]. Studies have observed that osteoarthritic humeral heads are morphologically different from normal humeral heads, with pathologic humeral head articular diameters found to be significantly greater than non-pathologic humeral head diameters [42]. Posterior glenoid erosion is another hallmark of glenohumeral OA [44]. This occurs as the humeral head subluxates postero-inferiorly leading to a biconcave appearance known as type B2 glenoid [44]. The B2 arthritic triad, which includes glenoid biconcavity, acquired glenoid retroversion, and posterior humeral head subluxation, represents one of the most challenging and controversial manifestations of shoulder OA [43].

1.4.3 Bone sclerosis

Sclerotic bone growths have been reported in the glenohumeral joint, particularly in the context of shoulder OA [82]. The relationship between bone sclerosis and OA is complex with evidence suggesting it can both contribute to and result from osteoarthritic process [82]. Sclerotic growth on bones refers to areas where bone tissue has become abnormally dense and hardened [82]. Subchondral sclerosis, which refers to the thickening and hardening of bone beneath the cartilage, is a recognized feature of OA, including in the glenohumeral joint [82]. Some studies suggest that subchondral sclerosis can occur before cartilage damage in OA, raising the possibility that it may be a contributor to the disease

process [**?**]. The emerging theory is that changes in bone structure might alter the biomechanics of the joint, leading to abnormal stress distribution and cartilage degradation [82]. Some research has pointed to the possibility that early subchondral bone changes might precede and contribute to cartilage damage. However, animal models and some human studies have suggested that alterations in subchondral bone, including sclerosis, can lead to or exacerbate cartilage damage [82]. The consensus is that while subchondral sclerosis might contribute to OA progression, it is more commonly viewed as a secondary response to the disease [82].

Sclerosis is generally considered a response to the mechanical stress and cartilage breakdown that occurs during OA. This process of subchondral sclerosis is the body's attempt to reinforce the joint [82]. However, this response can exacerbate joint stiffness and pain, further contributing to the degenerative cycle [82]. Overall, while bony sclerosis may be associated with shoulder OA, the exact nature of its role either as a primary driver or a secondary effect is still a subject of ongoing research. It is possible that there is a complex interplay between cartilage degeneration and bone changes in the development and progression of OA.

1.5 Overview of dual-energy CT technology

Dual-energy CT (DECT) operates by acquiring two image datasets of the same anatomical region using two different X-ray energy levels. This technique leverages the fact that tissues exhibit varying attenuation properties at different X-ray energies [18]. DECT scans can be acquired using two different kinds of scanners: Dual-source scanners are equipped with two X-ray tubes, which work at different voltages (high and low) to allow simultaneous acquisition of images at two different energy levels [12], while fast-switching kVp scanners, rapidly switch between high and low energy x-ray energies to sequentially gather images. DECT is superior to single-energy CT because of its ability to differentiate materials based on their chemical composition [12]. The generation of two images from different energy levels makes it possible to extract information and characterize the chemical composition of material based on the different degrees of X-ray beam absorption and attenuation according to the atomic weight electron density of the compounds [12]. Comparing attenuation values at high and low energy levels permits post-processing algorithms in DECT software to provide the basis for material decomposition [12]. There are three main approaches by which post-processing algorithms help discern materials: three material decomposition, Virtual non-calcium (VNCa) images, and two-material decomposition [18].

Three-material decomposition is primarily achieved in the image space domain [18].

The absorption characteristics of three materials e.g., iodine, soft tissue and air are examined, and the contribution of iodine is specifically ascertained [18]. Iodine data can then either be overlaid on the gray scale images as color maps or subtracted from the acquired dataset to generate virtual non-contrast images [18]. Three-material decomposition is helpful in estimating the concentration of elements like iodine, calcium, and iron [18]. The VNCa image approach is based on the three-material decomposition algorithm and is used for quantifying calcium deposits or their subtraction from areas of calcification that may be obscuring underlying structure [18]. Calcium signal can be removed from the images displaying cancellous bone to enable easy identification of lesions in the bone marrow space [4]. The VNCa technique is helpful in the detection of bone marrow lesions (BMLs) and therein evaluates calcium, yellow marrow, and red marrow by the three-material decomposition concept [18]. DECT with VNCa reconstruction is sensitive and specific in identifying traumatic BMLs in patients [4]. Finally, in two-material decomposition, the images are generated for two varied materials based on their respective atomic numbers and mass-attenuation coefficients [18]. This is effective for materials that have notable differences in their atomic numbers e.g., iodine and calcium or, iodine and water [18]. Different imaging techniques, such as DECT or simulated monochromatic images, offer different advantages in medical imaging due to their unique strengths. DECT scanners provide access to multiple energy levels (e.g., low 80 kVp and high 140 kVp images) that allow for improved material differentiation and soft tissue contrast, whereas simulated monochromatic images offer enhanced image quality through reconstruction of images to simulate them being acquired at a single energy level.

1.5.1 Simulated monochromatic images

Simulated monochromatic images, also known as virtual monochromatic images (VMI), are a key feature of DECT technology. These images encompass the benefits of imaging at high spectral energy (less beam hardening and streak artifacts) and low spectral energy (increased soft tissue resolution) [18].

The process of creating simulated images starts with DECT scanning. As scanning proceeds, the DECT scanner collects attenuation data across these two energy levels for each voxel in the body. Using the dual-energy data, the scanner can differentiate between different materials (e.g., bone, soft tissue, fat) within the scanned area based on their unique attenuation properties at different energy levels. Advanced algorithms and mathematical models are then applied to the image data using specialized software to decompose the mixed-material signal into its constituent components. Once materials are differentiated, the software synthesizes what the image would look like if it were to be captured using a

monochromatic X-ray beam at a specific energy level. The user or the software can then select the specific energy levels (e.g., 70 keV, 100 keV) to generate images.

Different energy levels can enhance or reduce the visibility of certain tissues or materials. Conventional CT uses a polychromatic X-ray beam that covers a broad spectrum of energies. The resulting images are influenced by the entire range of X-ray energies which can lead to artifacts such as beam hardening, where lower-energy X-rays are preferentially absorbed. Simulated images are created as if they were acquired with a monochromatic beam at a single energy level, thus reducing artifacts and improving image quality. One of the main problems with conventional CT is that it may show artifacts such as beam hardening, where denser materials (e.g., bone) cause lower-energy X-rays to be absorbed more leading to streaks or dark bands in the image. By selecting an optimal energy level, simulated images can reduce beam hardening artifacts and improve contrast resolution between different types of tissues, making them particularly useful for detecting joint and tissue changes in OA.

1.5.2 Density calibration phantoms

In quantitative computed tomography (CT), such as dual-energy CT (DECT), bone mineral density is commonly measured using a calibration phantom to convert the Hounsfield units (HU) of the CT image into density values [68]. During a CT scan, x-ray absorption by tissues is captured through linear attenuation profiles, which are represented by CT numbers. These values are then converted into Hounsfield units, with air (-1000 HU) and water (0 HU) serving as standard reference points [68]. A Hounsfield unit indicates the degree of x-ray attenuation in any voxel within the 3D image [68]. To derive bone mineral density from CT data, HUs are converted to units within the International System (e.g., mg/cm^3) [68]. Calibration phantoms for bones typically consist of rods made from materials with known densities that represent a range of tissues, including soft tissues (such as muscle or fat) and bone mineral equivalents (like calcium) [68]. The most commonly used calibration standards are solid (calcium hydroxyapatite) and liquid (dipotassium hydrogen phosphate, K_2HPO_4) [68].

Dipotassium phosphate (K_2HPO_4) is an inorganic compound composed of potassium, hydrogen, and phosphate ions, with varying degrees of hydration [58]. Calibration phantoms made from K_2HPO_4 are commonly used in imaging studies to simulate soft tissues or fluids due to their high water solubility and pH-buffering properties, making them well-suited for mimicking aqueous environments [17]. Hydroxyapatite (HA) is a naturally occurring mineral form of calcium apatite and serves as the primary inorganic component

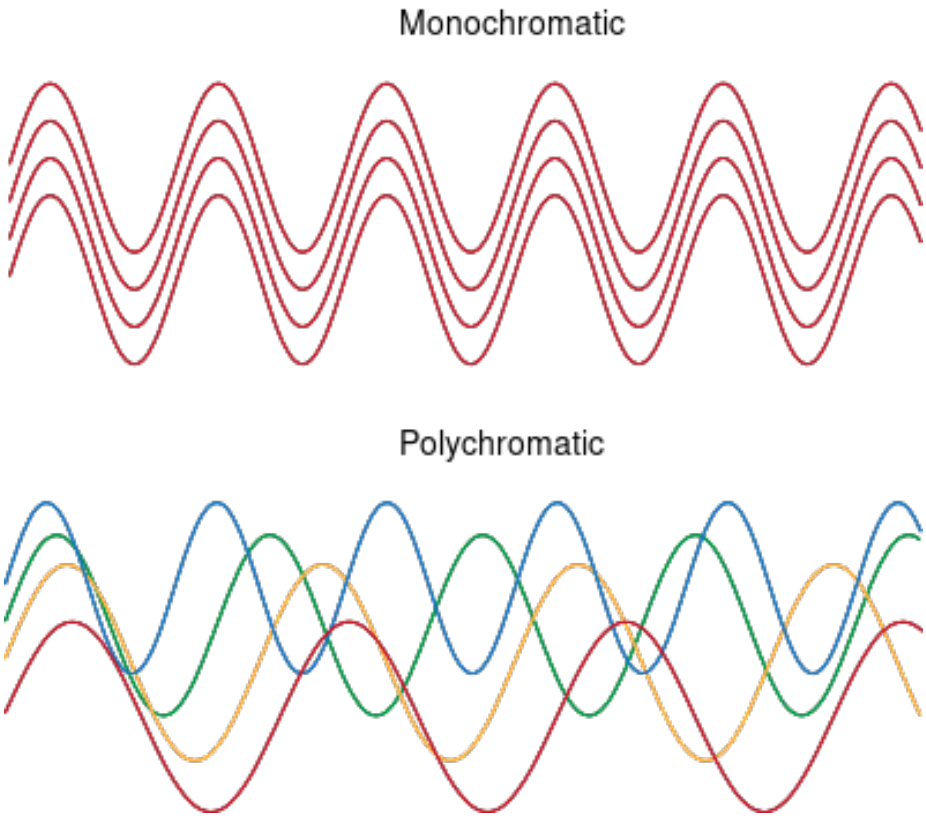


Figure 1.2: Comparison of the spectra of monochromatic and polychromatic X-ray beams [67].

of human bones and teeth [23]. HA-based phantoms are designed to replicate the physical and chemical properties of these hard tissues, making them valuable for studying bone mineralization, calcifications, and the behavior of surgical implants in imaging systems [23].

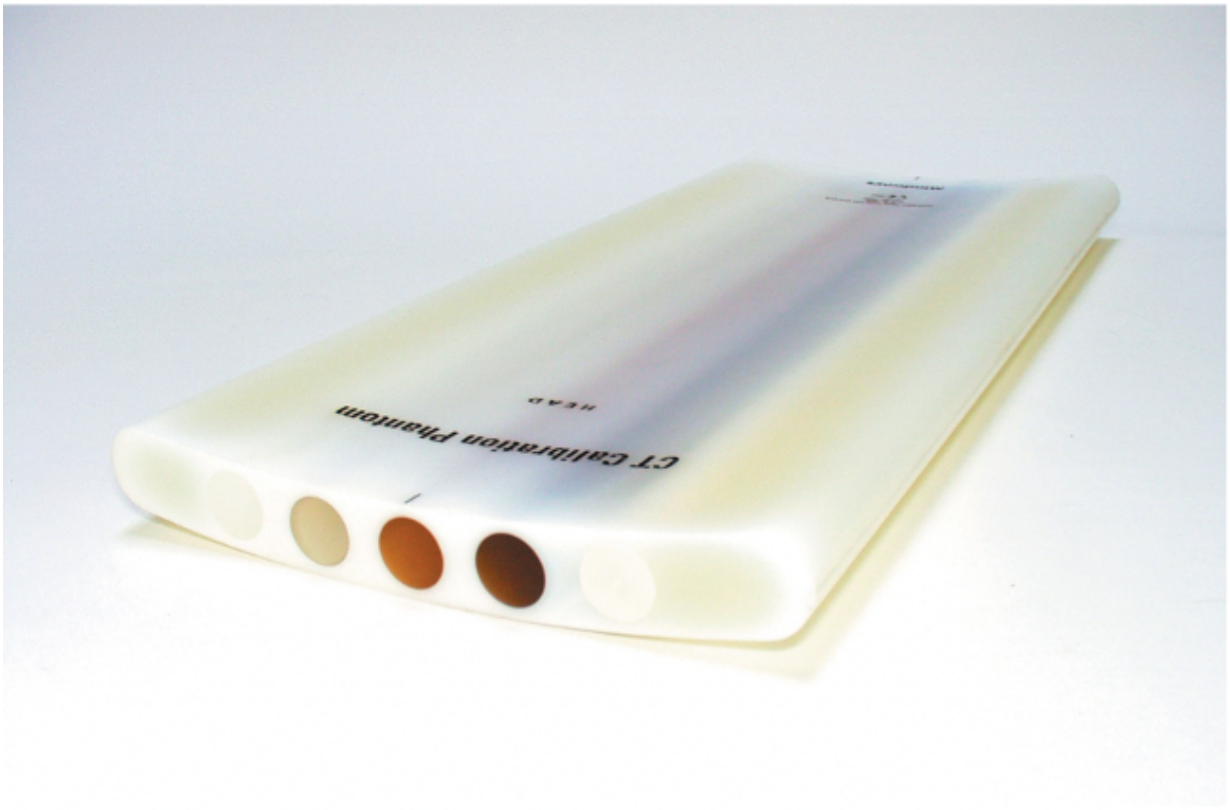


Figure 1.3: An example of a density calibration phantom [57].

1.5.3 Bone sharpening (BONE) and standard smoothing (STD) reconstruction kernels

Qualitative and quantitative DECT data can be altered by the choice of image reconstruction kernels. Reconstruction kernels are algorithms that help optimize image post-processing to improve the quality of images. The kernels modify the frequency content of the image data and allow sharpening or softening of the image based on the objective of the image in study [10]. The standard (STD) reconstruction kernel provides enhanced

image quality of soft tissues but does not specifically optimize the image for bone visualization, while the bone (BONE) reconstruction kernel provides bone edge sharpening, higher spatial resolution and better contrast for bone tissues, making it suitable for accurately detecting subtle bone abnormalities, fractures, or bone changes [87]. Kernels inherently alter both the qualitative and associated quantitative data and cannot be accounted for using standardized calibration phantoms alone [80]. This means that comparative studies or quantitative analyses must carefully consider the type of kernel used to ensure accurate and consistent results, as well as to mitigate potential biases introduced by the kernel choice. Additionally, these differences entail having tailored post-processing and analysis protocols to adequately interpret and utilize the DECT data in clinical and research settings. Figure 1.4 demonstrates how different energy pair combinations along with reconstruction kernels can be combined to create a singular DECT image.

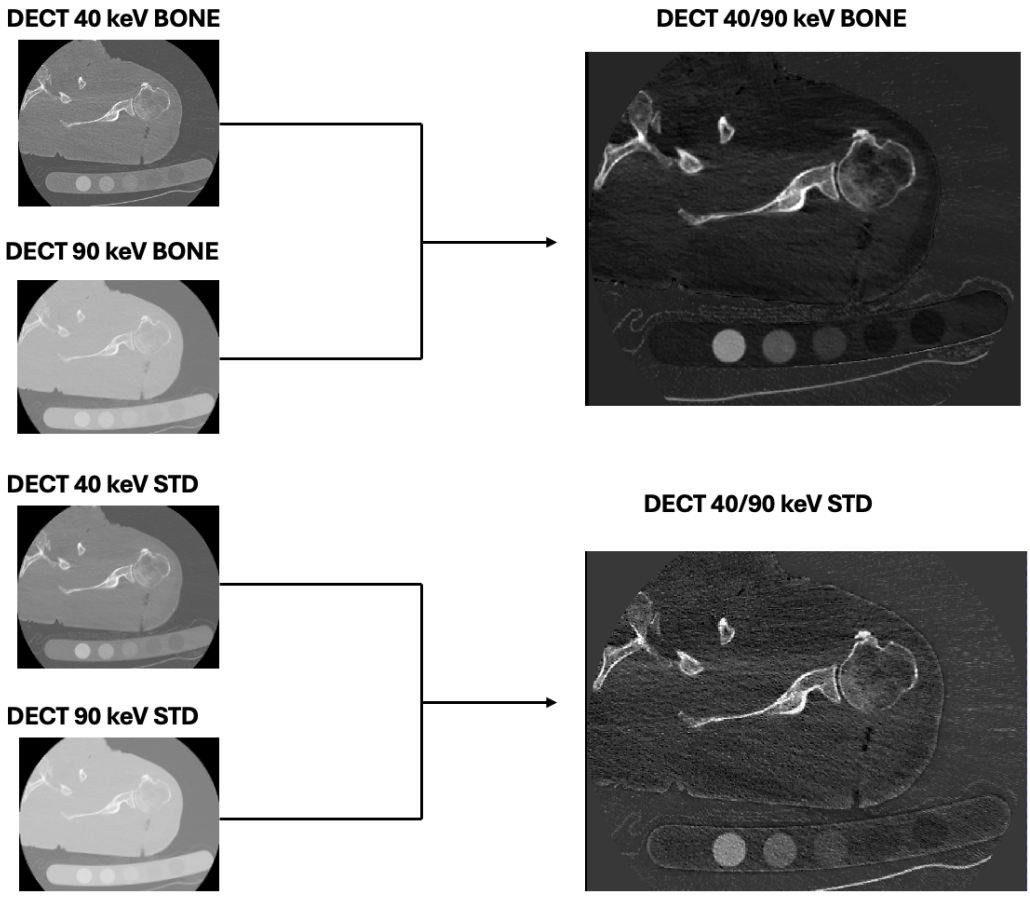


Figure 1.4: Representative axial DECT images of an isolated cadaveric shoulder generated using two reconstruction kernels (BONE and STD).

1.5.4 Volumetric bone mineral density

Volumetric bone mineral density (vBMD) is a measure of the density of minerals (e.g., calcium or hydroxyapatite) within a specific volume of interest. vBMD accounts for the depth of the bone and provides a density measurement relative to reference rods in a calibration phantom scanned with the object or subject. Due to spatial resolution limitations of clinical CT (including DECT), vBMD is not a true measure of bone mineral density, as it incorporates all materials within a specific voxel. As such, changes to the marrow space

or at the partial volume voxels at the edge of bone, result in over- or under-estimation of the bone's mineral content in a defined volume [38]. Voxel-specific errors in vBMD can be partially accounted for in DECT by utilizing the differences in energy attenuation information collected at the two separate energy spectra. This results in a "corrected" vBMD that minimizes the effects of marrow and other soft tissues on the vBMD measures. Material density estimations across tissues are required for using material decomposition methods, but it can be inherently challenging to fully correct for marrow or soft tissue changes alone. Proper characterization of the influence of marrow on vBMD measures is an ongoing area of research, and the current published methods will be used in this thesis [25, 34, 76]

There are several reasons for vBMD being an important measure for early detection of osteoarthritis. OA often begins with changes in the subchondral bone or from post-traumatic changes, such as fractures and dislocations. This alters the load distribution and joint mechanics of the bone, ultimately leading to alterations in the bone density and/or changes in the marrow space which are detectable through vBMD. By detecting changes in bone density and structure early, clinicians can implement early interventions to slow or halt the progression of OA in patients at high-risk [38]. Current strategies for early interventions to halt the initiation and progression of OA in weight-bearing joints such as in the knee and hip focus on decreasing joint pain while simultaneously restoring joint function [40]. These strategies can also be applied to early intervention of shoulder OA, and these interventions include synergetic therapy combining both long-term joint lubrication and drug intervention, regulatory balance between bone resorption and formation, and exercise therapy [40]. Accurate evaluation of vBMD is also important for modeling the mechanical properties of the bone, where vBMD is directly related to the elastic modulus in image-based finite element models.

1.5.5 Bone marrow lesions

BMLs are often associated with edema and inflammatory processes within the bone marrow as response to increased mechanical stress, injury, or degenerative changes [36]. BMLs are a common finding on MRIs, described as a change in bone marrow signal strength on MRI, with or without low T1-weighted and enhanced signal intensity on fluid sensitive sequences. BMLs appear as areas of increased signal intensity in T2-weighted and Short Tau Inversion Recovery (STIR) MRI sequences [36]. Traumatic bone marrow lesions (TBMLs) are post-traumatic bone marrow lesions combined with edema, bleeding, and fluid exudation due to acute trauma (e.g., bone contusion) or by overload-induced injury (e.g., stress fractures) [72]. TBMLs have been identified as useful clinical phenomenon that can help inform disease management, particularly as a potential target in precipitating OA [72].

Although MRI is considered the gold-standard preferred imaging modality for diagnosing TBMLs, DECT demonstrates excellent specificity in evaluating TBMLs in patients with acute injuries. However, DECT exhibits slightly lower sensitivity in detecting TBMLs when compared to MRI. Overall, the high diagnostic performance of the qualitative assessment of TBMLs using DECT is more feasible to perform in trauma settings and does not require additional time and effort as MRI. Since DECT has a high specificity and positive predictive value, the detection of TBMLs using DECT can help increase radiologists' confidence to diagnosis [72].

There are several classification systems for identifying the location and severity of TBMLs. Among these, the method developed by Costa-Paz et al. (2001) [22], displayed in Figure 1.5, is considered to be the most comprehensive assessment of TBMLs as it combines the appearance and location of the lesions and evaluates both the bone and cartilage non-invasively. Although TBML classification systems were based on MRI scans, their imaging appearance is similar to DECT or traditional CT imaging findings [72]. Table 1.1 provides the description of each type of lesion using the Costa-Paz classification system.

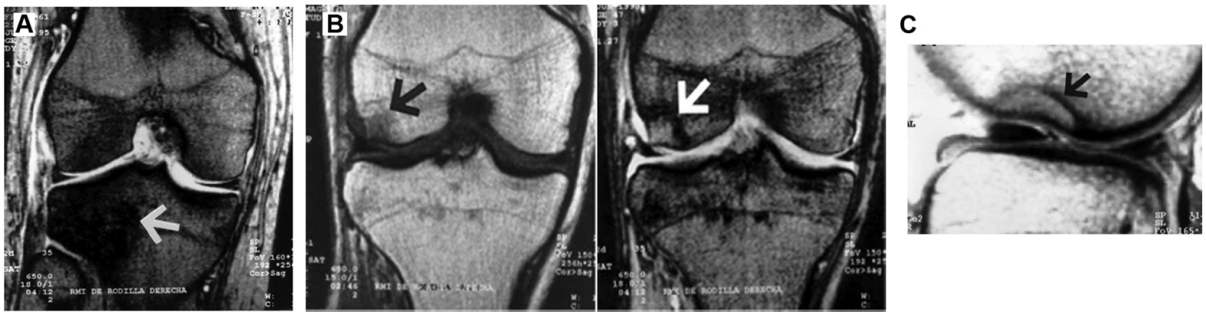


Figure 1.5: MRI scans identifying the Costa-Paz et al [22] subchondral TBML classifications in the knee; (A) type I lesion, diffuse signal with change of medullary component, can be reticular and distant from subjacent articular surface; (B) type II lesion, localized signal with contiguity to the subjacent articular surface, often crescentic in shape; (C) type III lesion, disruption of the normal contour of the cortical surface, often associated with type II lesions [74].

Table 1.1: Definition of the types of traumatic bone marrow lesions based on the Costa-Paz classification system [22, 74].

Type of lesion	**Definition**
Type I	Diffuse signal intensity with change of medullar component; often reticular and distant from subjacent articular surface.
Type II	Localized signal intensity with contiguity to articular surface; often crescenting lesions with varying thickness.
Type III	Disruption or depression of the normal contour of the cortical surface; often associated with type II lesions.

1.5.6 Finite element modeling

Finite element modeling (FEM) is a computational technique that can simulate the mechanical loading of bones. FE models can provide non-invasive, detailed insights into the mechanical behavior of bones that are otherwise difficult to obtain through experimental methods or average regional vBMD alone [90]. Generating a FE model of the proximal humerus can simulate its response to various loads and stresses, which can help us understand and determine disease progression and joint function in early stage OA. Early stage OA often involves the degeneration of the articular cartilage, in addition to the subchondral bone changes, which alters the load distribution across the joint [77]. FEM can simulate these changes and identify areas within the bone experiencing abnormal stress and strain that may contribute to cartilage breakdown. FEM helps in detecting these changes by modeling the mechanical response of subchondral bone under various loading conditions [77]. In CT image-based FEMs, bone elastic modulus is directly related to vBMD [47]. As such, accurate vBMD input to FEMs is essential to simulate accurate mechanical response of the bone. Given that DECT provides improved vBMD measures and can account for vBMD inaccuracies due to acute injury and disease, DECT-based FEMs may provide a significant improvement to current methods to determine early bone characteristics related to disease initiation and progression [47]. However, given DECT's relatively new integration in clinical care settings, DECT-based FEMs has yet to be described in a study other than Knowles et al. (2024) [47].

1.6 Clinical applications in MSK assessment

In MSK radiology, DECT has become a revolutionary imaging method [2]. The main advantage of DECT over conventional or single-energy CT is its ability to add clinically valuable information for a given anatomical part using material decomposition [2]. DECT has been used to accurately characterize bone marrow abnormalities, such as bone marrow lesions, and fatty infiltrations of the marrow [35]. DECT applications can be divided into the exploration of material-nonspecific and material-specific energy-dependent information, both of which can be qualitative or quantitative [35]. The former involves generating virtual monoenergetic imaging, creating effective atomic maps, and electron density maps, while the latter involves material decomposition, material labeling, and material highlighting [35]. Additionally, DECT has been utilized in clinical settings to better evaluate tissue composition and provide more precise quantification of tissue characteristics in MSK disorders and injuries.

Detection of occult fractures is a challenge on conventional x-rays and CT scans as subtle cortical, endosteal or trabecular injury patterns may not be apparent [18]. Such injuries can be made conspicuous using surrogate markers of injury like BMLs [18]. On a conventional CT, it is difficult to detect BMLs as increased attenuation of the lesion is confounded by the inherent attenuation of the trabecular pattern of the marrow space [18]. MRI is considered as the standard modality for identifying BMLs in acute settings, except for some of the limitations it poses (e.g., unstable patient in acute trauma, artifacts from metal hardware, and limited availability) [18, 12]. Metal implants in MRI do produce significant susceptibility artifacts in the images including beam hardening which occurs due to the rapid absorption of low energy photons in the spectra by the metal implant leaving behind high energy "harder" rays on the acquired image [18]. Metal implants in patients can also affect the quality of conventional CT images through varying proportion of photon starvation, photon scatter, edge effects, beam hardening, signal pile up, and excessive signal-to-noise ratio in images [18]. DECT reduces metal artifacts in images by using virtual monoenergetic techniques [18, 12]. Since CT scanners are generally more widely available than MRI machines in most healthcare settings, we can infer that DECT is also more readily available than MRI in acute settings [13]. Compared to MRI, DECT may also represent a valid imaging alternative in specific settings of acute spinal trauma and in follow-up examinations, especially in elderly or unstable patients and in cases of subtle or complex orientated fracture lines [13].

As such, DECT strikes a balance between conventional CT and MRI by demonstrating lower susceptibility to beam hardening artifacts, wider availability and having shorter wait times, being safer for unstable patients, and providing superior soft tissue visualization

without an increase in total radiation dose for the patient [18, 12].

1.7 Diagnostic performance and accuracy of DECT in identifying MSK injuries

In a study done by Gamala et al., 2019 [31] DECT was found to have good diagnostic accuracy in identifying established gout. Although MRI has been the reference standard for detecting BMLs in patients, BMLs can also be detected using DECT through three-material decomposition analysis [7]. Wilson et al., 2021 [83] found that DECT has excellent specificity for detecting BMLs in patients with acute knee injuries when using MRI as the reference standard. DECT has high overall diagnostic accuracy in depicting bone marrow lesions around the knee joint when compared to MRI, both in the acute and chronic settings [30]. Booz et al., 2019 [9] in their study involving 57 patients, reported a 94% sensitivity and 95% specificity, respectively, for identifying BMLs of the femur in the acute setting.

1.8 Comparative analysis of DECT with other imaging methods

DECT has been utilized to better evaluate tissue composition and provide more precise quantification of tissue characteristics [35]. These advancements in DECT technology can improve the diagnosis and assessment of MSK injuries [35]. DECT is useful in atypical presentations which pose a diagnostic challenge and distinguish it from other arthropathies and masses, such as septic arthritis, rheumatoid arthritis, osteoarthritis, pseudogout, or tumors [70]. It is also particularly useful in imaging anatomical sites that are not directly accessible for testing with fluid aspiration (e.g., gouty arthritis) [70]. A more recent application of DECT has been in the evaluation of inflammatory arthropathies. Early detection of inflammation is essential to initiate therapy and halt progressive damage to the affected tissues [70]. The most common use of DECT, however, has been to detect bone marrow lesions as a marker of subtle fractures which are not evident on radiographs or conventional CT images, especially in emergency setting or when MRI is contraindicated [70].

Most imaging modalities used in acute or emergency settings to evaluate MSK trauma, including x-rays, conventional single-energy, or mixed-energy CTs, are optimized to scrutinize the cortex of the bone [4]. Traditionally, CT utility is based on illustration of

attenuation characteristics of the body tissues while contrast-enhanced CT and MRI provide more physiologic information [18]. MRI is considered the mainstay and gold standard for detecting bone marrow lesions in clinical settings. The superior tissue characterization of MRI makes it ideal for identification of bone marrow processes, including bone marrow lesions [4]. However, MRI has several drawbacks: firstly, most traumatic injuries are evaluated in emergency departments where MRI is not conveniently available [4]. When it is, access to MRI may not be as easy and time sensitive as radiography or single-energy CT [4]. Additionally, MRI is more time intensive when compared to radiography or CT for patients in pain and distress, a shorter examination duration is often preferable [4]. Moreover, due to the high cost of multiple expensive protocols, long examination periods, and multiple contraindications, the application of MRI remains limited [89]. Similarly, single-energy CTs can visualize mineralized tissues but lack precision to stratify inflammatory MSK disorders [60]. Images can also be confounded by noise in the presence of bone marrow lesions, fatty infiltration or other joint alterations during injury or disease progression, requiring more advanced imaging approaches to detect early tissue damage and changes before they become permanent [26]. While accuracy may be somewhat improved with CT, which overcomes the 2-dimensional limitation of conventional X-rays, identifying the associated bone is critical to confidently diagnose acute traumatic injuries [4]. However, with conventional CT the identification of bone is limited by cancellous bone and single-energy x-ray spectra [4].

Overall, DECT is a viable option for evaluation of acute MSK trauma [4]. Conventional CT evaluation can often be limited by beam hardening, photon starvation, partial volume averaging, and scatter [70]. Standard techniques for mitigating these effects include high tube voltage or current, applying smoothing filters, or applying iterative reconstruction algorithms [70]. However, these techniques have trade-offs, including a higher radiation dose, lower spatial and contrast resolution, and reconstruction errors [70]. As such, DECT presents certain advantages which have increased its utilization in acute care setting. DECT techniques rely on the principle that as X-ray energy changes, varied materials attenuate x-rays to different degrees [4]. Using post-processing software, materials with major differences in effective atomic number can be uniquely classified, providing material decomposition and better visualization of bones and soft tissue contents [4].

1.9 Cost effectiveness of DECT

MRI may not be accessible in hospitals, is more expensive than other imaging modalities, and may be contraindicated in some patients [52]. This contrasts with CT, which is more

readily available, cheaper, and safer [52]. MRI also has a long inpatient waiting time with an audit revealing an average waiting time of 36 hours globally, leading to delayed diagnosis and treatment and prolonged length of stay [52]. DECT may be performed at the same setting and in addition to single-energy CT (SECT) on the same machine, making it more cost-effective than just performing SECT on its own [52].

Switching imaging modality from MRI and SECT to DECT will both decrease cost, in terms of the costs of the scan and of inpatient hospitalization and improve patient outcomes with reduced rates of mortality and morbidity [52]. The lower cost of DECT results from its high specificity, which leads to a lower incidence of false positives, and thus lower chances that the patient undergoes unnecessary treatment [64]. Emergency department imaging, which focuses on delivering timely and accurate reports, is an area where dual-energy imaging should provide a unique advantage [79]. In a study by Wong et al. (2020) [85], image findings from DECT avoided approximately 191 total recommended follow-up MRI examinations and 21 to 28 total CT examination requests. They projected the overall net cost reduction on the healthcare system was approximately $50,000 to $60,000 [85]. While the reduction in downstream costs is significant, it is important to note the increased confidence the radiologists felt in diagnosing patients in the emergency department where their interpretations are critical for timely management of patients [85].

1.10 Challenges and limitations in the use of DECT

One of the challenges of using DECT includes scanning patients with larger physique, which can cause beam hardening of images obtained using the low energy x-ray tube [4]. This beam hardening can potentially limit the quality of the source and VNCa images produced from DECT [4]. Additionally, normal red marrow and red marrow reconversion have higher CT attenuation on VNCa images and can confound findings of true bone marrow lesions [4]. Automated reconstruction of VNCa images is now available, eliminating the need for time-consuming postprocessing by the technologist or radiologist on a thin-client workstation, with images automatically exported to picture archiving and communication system (PACS) for image evaluation [4].

Physiological excessive red marrow in axial skeleton or, areas of marrow hyperplasia (red marrow re-conversion) in the appendicular skeleton can result in false positive imaging results for BMLs on DECT as the attenuation of red marrow is higher than fatty yellow marrow and almost nears that of water. BMLs in the immediate vicinity of cortical bone may get masked by space averaging corrections done by the software, leading to false negative imaging results. Additionally, in individuals with increased body weight undergoing

imaging for areas like the hip, arm by the side or spine, the lower energy x-rays may not penetrate effectively, leading to photon starvation and sub-optimal signal to noise ratio on the acquired DECT images. Another challenge while using the dual-source scanner in patients with higher body mass can be the limited field of view (FOV) in the high energy detector assembly beyond 33–35 cm. Incorrect window or level settings can lead to false positive imaging findings of BMLs. DECT images and algorithms of BMLs detection may get affected in presence of large and dense metallic implants by excessive beam hardening, photon starvation and streak artifacts [18].

Monochromatic images allow for enhanced tissue differentiation and contrast as they represent the attenuation characteristics of tissues at specific photon energy levels. Lower energy images provide increased contrast for soft tissues due to the higher photoelectric absorption coefficients, but may encounter challenges when assessing the shoulder region in DECT due to attenuation by the torso. The torso consists of denser structures like bones and organs which can attenuate the X-rays before they reach the shoulder region during DECT image acquisition. As a result, lower energy images may suffer from decreased penetration and increased scatter, leading to artifacts and decreased visibility of structures in the shoulder. In order to mitigate these attenuation issues, higher energy monochromatic images can be employed. These images offer greater penetration through the torso and are less affected by attenuation, providing clearer visualization of the shoulder anatomy.

1.11 Research objectives and aims

Previous research studies have been conducted to compare vBMD and FEM estimated stiffness in the proximal humerus sections from cadaveric shoulders [47]. These comparisons were based on images obtained with SECT and DECT scans, which were reconstructed using BONE and STD kernels [47]. However, research is needed to compare vBMD and FEM estimated stiffness in the proximal humerus using DECT images reconstructed with BONE and STD kernels at various high and low energy pair combinations.

This study investigated whether the effect of different high and low DECT energy pair combinations on vBMD and FEM estimated stiffness could be used as an initial step toward developing image-based biomarkers for the early detection of OA-related changes in the proximal humerus. DECT was used to measure vBMD and model bone stiffness and loading with FEM in cadaveric models. DECT image-based characteristics were assessed at baseline for all of the cadavers and participant cohort. Specifically, localized regions of the proximal humerus were used to determine vBMD and bone stiffness (cadavers and participants) using DECT BONE/STD reconstruction kernels. The sections compared

included: the humeral shaft diaphysis, articular surface of the humerus (humeral head), and the anatomical neck (Figure 1.6). Sections were chosen to represent regions with high cortical bone (humeral shaft) and trabecular bone (anatomical neck and articular surface), as well as a region that exhibited adaptive bone changes due to acute injury and disease progression (articular surface of humerus). Figure 1.7 highlights the order of steps that were taken for this project.

Throughout the course of this study, software and image processing techniques were developed that used DECT images to distinguish changes in tissues of varying density, to allow concurrent measurements using a single clinically available imaging modality and reduce the influence of noise. The specific aims were:

1. Compare the effects of varying energy pair combinations of DECT images (40/90, 90/140, 40/140 keV) on the vBMD in cadaveric models and participants.

2. Compare the effects of varying energy pair combinations of DECT images (40/90, 90/140, 40/140 keV) as input to image-based FEMs on bone stiffness in cadaveric models and participants.

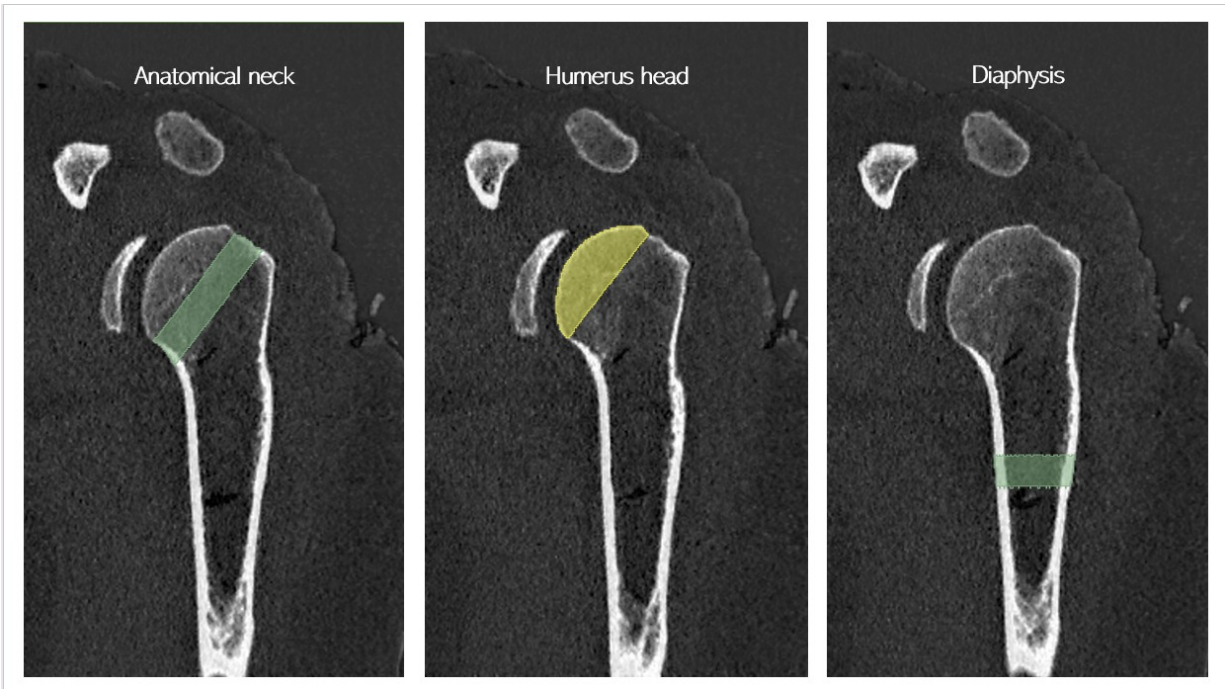


Figure 1.6: DECT scans overlaying sections of the proximal humerus that were analyzed.

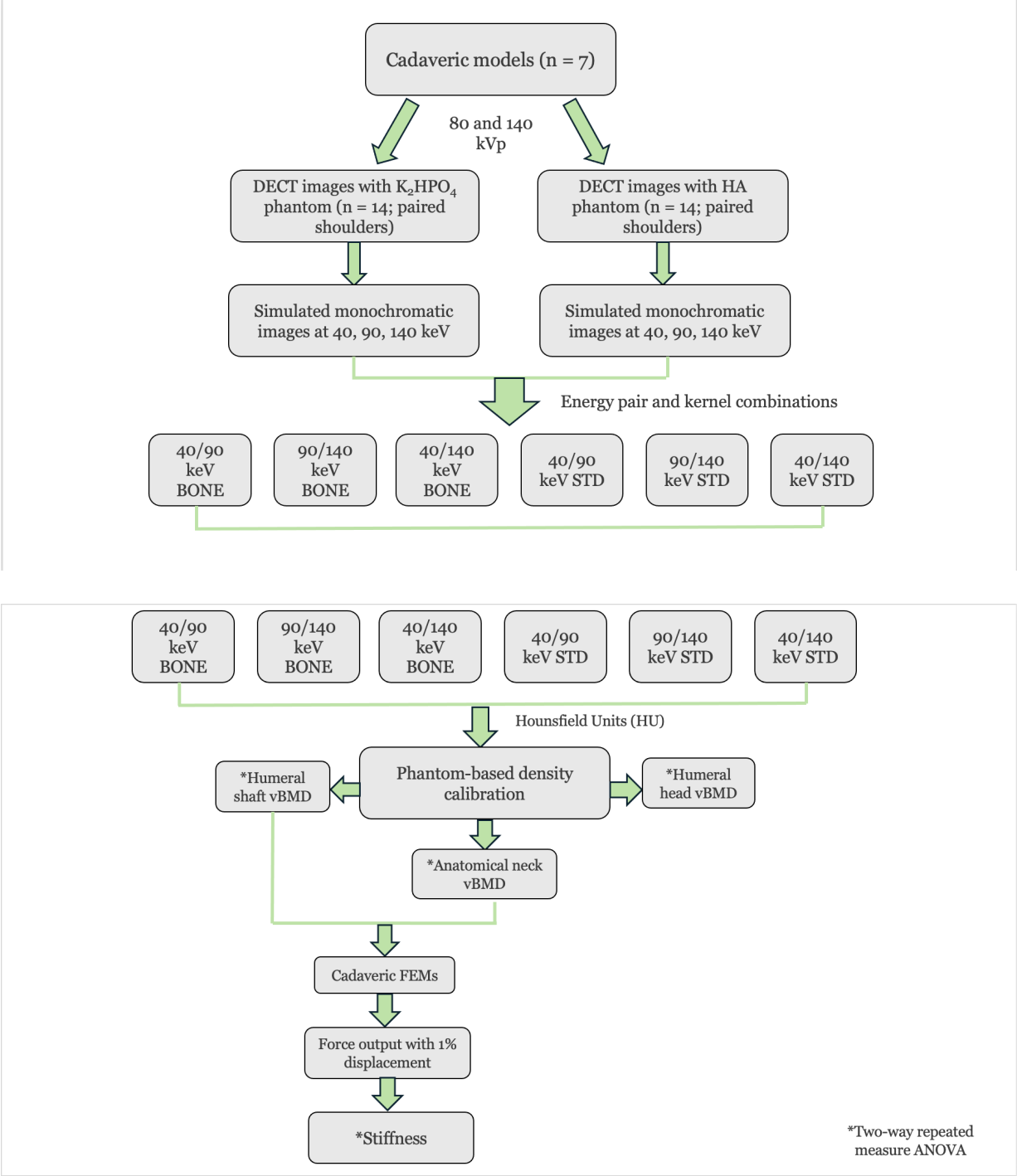


Figure 1.7: Flowchart displaying order of steps taken in the study, along with the relevant statistical measurements.

1.12 Hypothesis

The hypotheses for this study were as follows:

- The highest energy pair combination 90/140 keV and BONE kernel image will show higher vBMD values compared to the lower energy pairs (40/140 and 40/90 keV) and STD kernel images.
- The highest energy pair combination 90/140 keV and BONE kernel image will show higher stiffness values compared to the lower energy pairs (40/140 and 40/90 keV) and STD kernel images.

Chapter 2

Methodology

2.1 Participants

1. ***Cadaveric specimens:*** Cadaveric specimens (n = 7; 14 shoulders) were scanned bilaterally using DECT and used to optimize DECT imaging protocols and parameters. Of the seven cadavers, five had their entire upper thorax and shoulders maintained while two had right and left shoulders removed due to size constraints during travel and scanning. The study sample of cadavers consisted of a mix of male and female specimens, with ages ranging from 55 to 96. Details of the donor specimen ID, age, and sex is included below (Table 2.1).

Table 2.1: Demographic characteristics and sectioning of cadaver specimens being scanned for study.

Donor ID	Sex	Age	Section
23162	F	55	Right and Left Shoulders
23163	M	73	Right and Left Shoulders
23167	M	83	Thorax and Shoulders
23168	F	96	Thorax and Shoulders
23169	F	93	Thorax and Shoulders
24170	M	90	Thorax and Shoulders
24175	M	78	Thorax and Shoulders

2. ***Patient eligibility:*** Participants for this study were recruited at the Roth|McFarlane Hand and Upper Limb Centre and the Emergency Department at St. Josephs Health Care, London, ON within the first six (6) weeks of first-time traumatic shoulder dislocation. Clinical diagnosis was confirmed based on the injury mechanism and standardized clinical tests. Participants were also clinically diagnosed for the presence of prior or current bone loss, fractures, or instability as part of the exclusion criteria for the study. Baseline images were captured for three participants with 6-month follow up scanning conducted for two of the participants.

    - ***Inclusion criteria:*** Adult males aged 18 to 45 with first-time traumatic shoulder injury. Participants with combined soft-tissue injuries were also included.
    - ***Exclusion criteria:*** Participants with significant humeral or glenoid bone loss (engaging Hill-Sachs lesions, large glenoid defects with cartilage disruption), intra-articular fractures, recurrent anterior shoulder instability ($\geq$ 2 dislocations/subluxation events in the past year), history of steroid or bisphosphonate use. Female participants were not recruited for this study to minimize unnecessary exposure to radiation. Since this research involves imaging the upper body, including the thorax region, our aim was to reduce the potential risks associated with radiation in female patients given the exploratory nature of this research.

2.2 Medical imaging

DECT imaging was performed on the cadaveric models and on the affected shoulder of participants at baseline (within 6 weeks from onset of injury) and at 6-month follow-up. All scans were completed on a fast switching x-ray tube multidetector CT scanner (Revolution CT, GE Healthcare, Waukesha, WI) by a medical radiation technologist using a standardized clinical shoulder protocol. Scans captured a minimum of four 40 mm image stacks consisting of the entire glenohumeral joint within the scan FOV (80 kVp and 140 kVp, 0.488 mm x 0.488 mm x 0.625 mm). A hydroxyapatite (HA) calibration phantom (QRM-50125, QRM Phantoms, Möhrendorf, Germany) was placed under the shoulder in scans for quantitative image analysis of bone density in both the cadaver specimens and the participant cohort. Shoulder scans were also obtained from cadavers using a liquid dipotassium phosphate ($\mathbf{K_2HPO_4}$) (Model 3, Mindways Software, Austin, TX, USA) calibration phantom. Images were subsequently reconstructed using the DECT BONE and STD reconstruction kernels. Manufacturer-provided software (Gemstone Spectral Imaging (GSI), GE Healthcare) was then used to generate simulated images at 40, 90, and 140 keV

and combined to form DECT images of low and high energy pairs of 40/90 keV, 90/140 keV, and 40/140 keV. All medical imaging was performed at St. Joseph's Health Care, London, Ontario.

2.3 Image processing and volumetric bone mineral density (vBMD) analysis

The high attenuating nature of imaging through the torso requires different energy monochromatic images to be used, and this was tested for as part of the study design using the cadaveric models (study aim 1). Firstly, DECT images were created from the reconstructed simulated monochromatic images using a custom Python code [25], modified to include the use of $\mathbf{K_2HPO_4}$ and HA phantom rods, at 40, 90 and 140 keV for the cadaver samples. The custom code uses linear regression between the low- and high-energy images to generate a single DECT image in calibrated $\mathbf{K_2HPO_4}$ or HA density. Calibrated DECT BONE and STD images were used for vBMD analysis and the $\mathbf{K_2HPO_4}$ images were used as input to image-based FEM for bone stiffness and loading measures. This is because the density-modulus relationship for image-based FEMs is governed by $\mathbf{K_2HPO_4}$-derived relationships, as such using HA-equivalent density adds little value to the results [58, 62].

Stage one: Cadaver specimens

In the first stage of this study, the following specific image comparisons were made using the cadaveric models:

1. vBMD comparisons in the humeral shaft diaphysis, anatomical neck of humerus, and articular surface of humerus (humeral head) using DECT BONE/STD reconstruction kernels derived from 40/90 keV, 40/140 keV, and 90/140 keV using, a) $\mathbf{K_2HPO_4}$ and b) HA phantom-calibrated images,

2. FEMs of bone stiffness and loading in the humeral shaft diaphysis and anatomical neck of the proximal humerus of cadaver specimens using the three image combinations (40/90 keV, 40/140 keV and 90/140 keV) and two reconstruction kernels (BONE and STD) as vBMD input.

Stage two: Participants

Subsequent image analysis was performed in the baseline images of all three participants and 6-month follow up analysis on two of them using the associated parameter combination:

1. vBMD comparisons in the humeral shaft diaphysis, anatomical neck of humerus, and articular surface of humerus of participants using DECT BONE/STD reconstruction kernels derived from HA phantom-calibrated images.

2. FEM of bone stiffness and loading in the humeral shaft diaphysis and anatomical neck of the proximal humerus.

For the first objective of this study, phantom-based density calibration was applied to the DECT images from the 14 bilateral cadaveric shoulder specimens and participant scans to derive vBMD measurements. Simulated monochromatic CT images were initially collected and reconstructed using the BONE and STD reconstruction kernels. The DICOM files for these images were imported into ITK-SNAP (v.3.8.0) to convert them into MHA (metaimage) format, ensuring consistent image dimensions. ITK-SNAP [88] was also used to create K_2HPO_4 and HA masks for each donor specimen and participant based on the calibration phantom rods positioned beneath the shoulder. Once converted to MHA format, the DECT images, along with their respective calibration phantom masks, were processed using a custom Python script. This script, based on the methods of de Bakker et al. (2022) [25], combined the simulated DECT images into high- and low-energy pair combinations (40/90, 90/140, and 40/140 keV) (Appendix A.1).

Energy pair DECT images were subsequently imported into 3D Slicer software (v. 5.6.2) for segmenting the four regions of the proximal humerus. A mask was generated to create a 3D model of the proximal humerus, where a 10 mm STL segment was then placed and positioned to isolate the diaphysis and anatomical neck. To isolate the humeral head, a 75 mm STL segment was positioned on top of the 10 mm STL segment at the anatomical neck. Boolean intersection operations were then performed to isolate and create the desired 10 mm segments of the humerus. The anatomical neck and diaphysis segments were saved for further finite element analysis. Finally, vBMD values calibrated in K_2HPO_4 or HA units were extracted from the 10 mm segments isolated from the proximal humerus using 3D Slicer. Figure 2.1 illustrates the workflow for vBMD extraction from DECT images.

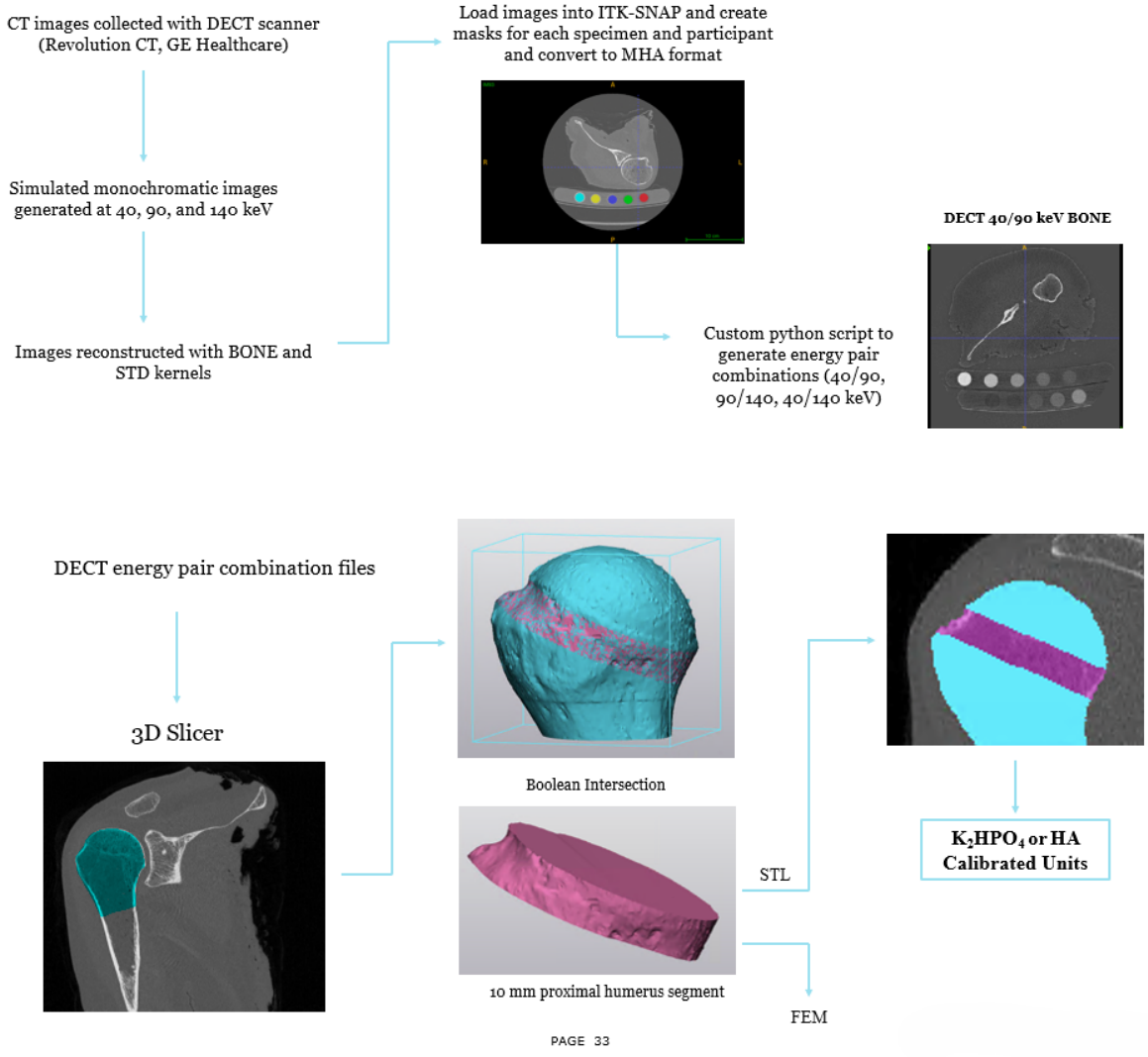


Figure 2.1: Stages of volumetric bone mineral density analysis and input to image-based finite element models for the study.

2.3.1 Finite element model (FEM) generation

For the second objective, FEM analysis for bone stiffness were run using the **K_2HPO_4**-calibrated vBMD images obtained in the previous objective for the humeral shaft and anatomical neck segments.

To create the FEM, a triangular mesh of elements was applied to the 10 mm segment from 3-matic, with a maximum edge length of 2 mm and geometrical accuracy confirmed using semi-automated tools (3-Matic v.16.0, Materialise, Leuven, BE). The segment was then brought into Abaqus (v.2022, Simulia, Providence, RI, USA) where a tetrahedral volume mesh was created. The density-modulus relationship [27] was then applied to this mesh using open-source material mapping software (Bonemat v.3.2) [78] which links the calibrated vBMD data in K_2HPO_4 density to the elastic modulus of the bone. The FEM was then imported back into Abaqus and a 1% apparent strain (or a 0.1 mm displacement) was applied to the FEM at a single node which will be tied to all nodes on the medial surface. The reaction force on lateral surface nodes from the applied strain was used for stiffness calculation. Stiffness was calculated by taking the calculated reaction force over the applied displacement.

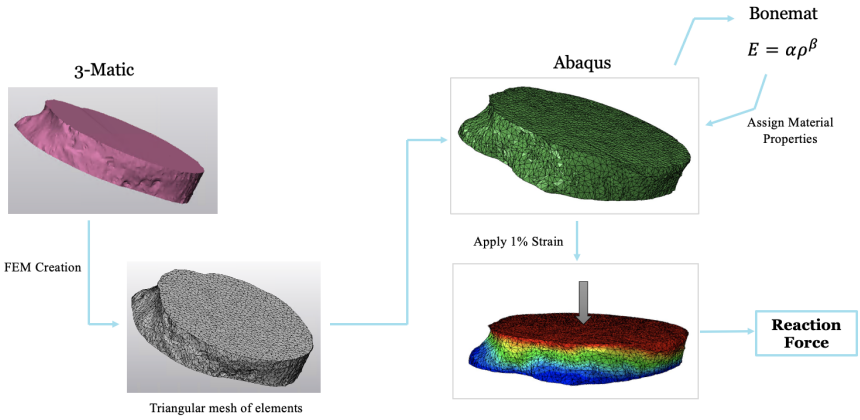


Figure 2.2: Stages of finite element model analysis for the study.

2.4 Statistical analysis

vBMD and stiffness of the proximal humerus sections scanned with **K_2HPO_4** or HA calibration phantoms were reported in the cadaver specimens and participants at each

energy pair combination (40/90, 90/140, and 40/140 keV). The average values for vBMD and stiffness were compared using a two-way repeated measures analysis of variance (RM-ANOVA) using R programming language. The two factors were the reconstruction kernel (BONE/STD) and the energy pair (40/90, 90/140, 40/140), which allowed us to determine if there were any differences between the means of each of the six groups. Linear regression was run for DECT BONE and STD image vBMD vs. stiffness values on each energy pair combination to compare slope, intercept, and R^2 and to determine whether vBMD was a good predictor of stiffness. Linear regression was also performed for each anatomical location of the proximal humerus, energy pair, and kernel to determine correlations between K_2HPO_4 and HA vBMD. The significance for all statistical comparisons was set to $p < 0.05$.

Chapter 3

Results

Tables 3.1 to 3.18 present the vBMD and FEM stiffness values for cadaveric specimens (n = 14) and recruited participants (n = 3). Among all energy pair combinations and reconstruction kernels, the highest average vBMD and FEM stiffness values were observed with the 90/140 keV energy pair using the BONE kernel, regardless of the calibration phantom type. Significant differences in average vBMD and FEM values ($p < 0.05$) were found between the BONE and STD reconstruction kernels across all three energy pairs in the humeral shaft diaphysis of cadaveric specimens, for both K_2HPO_4 and HA calibration phantoms. The lowest vBMD and FEM stiffness values were observed in the anatomical neck of the proximal humerus. However, no significant differences in mean vBMD and FEM values were detected across energy pair combinations for the humeral head or anatomical neck. Linear regression was also performed between vBMD and stiffness within each energy pair combination to determine how well FEM stiffness is predicted by vBMD, with comparisons between kernels (BONE and STD).

3.1 Cadaver specimens vBMD results

Using the K_2HPO_4 calibration phantom, significant differences in vBMD were observed between all energy pair combinations within the diaphysis using BONE kernel images ($p < 0.0001$) (Table 3.1). For STD kernel, significant differences were found between 40/140 keV vs. 90/140 keV and 40/90 keV vs. 90/140 keV ($p = 0.0067, 0.0051$), while 40/140 keV vs. 40/90 keV was not significant ($p = 0.0817$) in the diaphysis (Table 3.1). Interaction effects in this region also showed significant BONE vs. STD differences at BONE 90/140

keV and STD 40/90 keV ($p < 0.0002$) (Table 3.1). No significant differences in K_2HPO_4 vBMD were detected in the anatomical neck or humeral head (Table 3.4 and Table 3.6).

With the HA phantom, all BONE kernel image comparisons were significant in the diaphysis ($p < 0.001$) (Table 3.2). For STD kernel images, significant differences were found between 90/140 keV and both 40/140 keV and 40/90 keV ($p = 0.006$, 0.0079) in the diaphysis (Table 3.2). Significant differences were also noted in the interaction effects between BONE and STD images across BONE 40/90 vs. STD 40/140 ($p = 0.00012$) and BONE 90/140 keV vs. multiple STD energy pairs ($p < 0.05$) (Table 3.2). As with K_2HPO_4, no significant differences were observed in the anatomical neck or humeral head (Table 3.3 and Table 3.5).

Table 3.1: Volumetric bone mineral density (vBMD) in the **humeral shaft diaphysis of cadaver specimens** derived using two dual-energy CT reconstruction kernels with three energy pair combinations using the $\boldsymbol{K_2HPO_4}$ calibration phantom.

	Model	40/90 keV		90/140 keV		40/140 keV	
		BONE	STD	BONE	STD	BONE	STD
vBMD [mgK_2HPO_4/cc]	**23162L**	318.20	354.66	432.94	379.55	335.03	359.66
	23162R	319.84	352.78	425.68	374.20	332.84	355.75
	23163L	354.35	392.76	475.40	423.43	365.51	392.83
	23163R	334.83	376.32	457.00	405.22	349.47	376.05
	23167L	514.30	530.13	608.61	544.11	526.94	531.80
	23167R	484.54	495.99	560.69	506.51	493.56	497.31
	23168L	346.11	339.62	427.32	347.67	355.78	340.60
	23168R	305.26	312.80	397.28	317.24	316.12	313.35
	23169L	223.70	206.80	248.99	206.79	226.83	206.83
	23169R	216.50	199.64	235.42	199.53	218.94	198.94
	24170L	187.66	171.73	206.49	171.45	189.91	171.70
	24170R	203.06	185.92	221.03	185.79	205.20	185.91
	24175L	408.45	407.49	478.00	414.04	416.74	408.24
	24175R	432.32	437.95	520.99	451.90	442.81	439.61
	Average ± SD	**332.08 ± 102.54**^{a,b}	**340.33 ± 114.14**^{d,f}	**406.84 ± 130.15**^{a,c,f,g,h}	**351.96 ± 120.76**^{d,e,g}	**341.11 ± 105.53**^{b,c}	**341.33 ± 114.77**^{e,h}

Average values sharing a common letter are significantly different using a two-way RM-ANOVA (a, b, c, f, g, h: $p < 0.05$; d: $p = 0.0051$; e: $p = 0.0067$).

Table 3.2: Volumetric bone mineral density (vBMD) in the **humeral shaft diaphysis of cadaver specimens** derived using two dual-energy CT reconstruction kernels with three energy pair combinations using the **HA** calibration phantom.

	Model	40/90 keV		90/140 keV		40/140 keV	
		BONE	STD	BONE	STD	BONE	STD
vBMD [mgHA/cc]	**23162L**	319.05	352.44	421.57	373.41	331.25	354.92
	23162R	315.96	349.26	413.01	368.88	327.52	351.58
	23163L	347.59	384.65	465.47	418.80	361.62	388.69
	23163R	332.23	369.02	446.25	400.40	345.80	372.77
	23167L	503.25	542.37	594.04	551.33	515.29	536.97
	23167R	472.02	498.91	548.20	509.87	482.02	500.13
	23168L	333.47	334.01	410.16	340.82	342.34	334.81
	23168R	299.81	313.02	385.85	317.43	309.46	313.55
	23169L	219.17	204.11	242.01	204.49	223.17	204.38
	23169R	214.10	197.13	227.45	197.11	214.89	197.13
	24170L	190.14	177.01	207.46	176.78	192.20	176.98
	24170R	205.31	188.16	222.80	188.13	207.38	188.17
	24175L	418.72	426.93	490.24	433.93	427.25	427.74
	24175R	425.06	443.93	509.75	458.15	435.05	445.62
	Average ± SD	**328.28 ± 99.78^{a,b}**	**341.50 ± 116.64^{d,f}**	**398.88 ± 127.21^{a,c,f,g,h}**	**352.82 ± 122.41^{d,e,g}**	**336.80 ± 102.96^{b,c}**	**342.39 ± 116.41^{e,h}**

Average values sharing a common letter are significantly different using a two-way RM-ANOVA (a, b, c, f, g, h: $p < 0.05$; d: $p = 0.0079$; e: $p = 0.0060$).

Table 3.3: Volumetric bone mineral density (vBMD) in the **anatomical neck of the humerus of cadaver specimens** derived using two dual-energy CT reconstruction kernels with three energy pair combinations using the **HA** calibration phantom.

	Model	40/90 keV		90/140 keV		40/140 keV	
		BONE	STD	BONE	STD	BONE	STD
vBMD [mgHA/cc]	**23162L**	137.98	132.65	138.62	132.36	138.05	132.63
	23162R	133.91	127.39	135.97	127.47	134.15	127.40
	23163L	104.78	99.25	105.28	98.98	104.85	99.23
	23163R	86.24	79.51	86.78	79.35	86.29	79.48
	23167L	202.75	206.26	204.89	205.86	203.07	205.94
	23167R	173.68	170.97	173.54	170.89	173.27	171.02
	23168L	95.27	89.12	94.80	89.04	95.37	89.15
	23168R	85.65	78.07	85.52	77.95	85.44	77.96
	23169L	119.66	114.98	119.58	114.91	119.51	114.95
	23169R	95.53	85.79	95.61	85.36	95.87	85.45
	24170L	90.61	88.94	91.00	88.74	90.64	88.92
	24170R	86.37	81.35	86.91	81.54	86.43	81.15
	24175L	88.73	84.28	88.67	83.98	88.86	84.27
	24175R	110.77	106.41	110.06	106.84	110.49	106.69
	Average ± SD	**115.14 ± 35.88**	**110.36 ± 38.08**	**115.52 ± 36.32**	**110.23 ± 38.04**	**115.16 ± 35.88**	**110.30 ± 38.06**

No significant differences between average values were found.

Table 3.4: Volumetric bone mineral density (vBMD) in the **anatomical neck of the humerus of cadaver specimens** derived using two dual-energy CT reconstruction kernels with three energy pair combinations using the $\boldsymbol{K_2HPO_4}$ calibration phantom.

	Model	40/90 keV		90/140 keV		40/140 keV	
		BONE	STD	BONE	STD	BONE	STD
vBMD [mgK_2HPO_4/cc]	**23162L**	126.17	123.01	126.73	122.62	126.22	122.97
	23162R	124.58	117.89	126.39	117.60	124.80	117.86
	23163L	91.56	87.71	91.38	87.45	91.53	87.66
	23163R	72.72	67.00	73.31	66.19	72.79	66.90
	23167L	197.78	197.62	197.89	197.71	198.07	197.75
	23167R	175.74	174.01	174.92	173.43	175.45	173.68
	23168L	82.83	81.52	82.09	81.30	82.83	81.64
	23168R	72.71	68.97	72.06	68.52	72.81	69.02
	23169L	112.43	110.81	112.29	110.55	112.37	110.51
	23169R	90.76	86.77	90.50	86.40	90.86	86.63
	24170L	79.81	79.77	80.21	79.44	79.79	79.73
	24170R	77.53	78.62	77.99	78.34	77.95	78.40
	24175L	87.31	88.06	87.21	87.59	87.38	87.83
	24175R	108.88	111.61	109.03	111.48	109.06	111.64
	Average ± SD	**107.20 ± 38.34**	**105.24 ± 38.68**	**107.28 ± 38.35**	**104.90 ± 38.77**	**107.28 ± 38.32**	**105.16 ± 38.68**

No significant differences between average values were found.

Table 3.5: Volumetric bone mineral density (vBMD) in the **articular surface of the humerus head of cadaver specimens** derived using two dual-energy CT reconstruction kernels with three energy pair combinations using the **HA** calibration phantom.

	Model	40/90 keV		90/140 keV		40/140 keV	
		BONE	STD	BONE	STD	BONE	STD
vBMD [mgHA/cc]	**23162L**	206.74	201.29	206.46	201.04	206.68	201.26
	23162R	185.21	183.35	185.19	183.39	185.20	183.36
	23163L	171.68	166.23	172.05	165.98	171.72	166.21
	23163R	151.94	145.62	151.87	145.58	151.94	145.61
	23167L	334.53	331.16	334.91	331.02	336.41	331.26
	23167R	206.04	203.06	206.22	202.94	206.05	202.95
	23168L	198.51	196.54	198.12	195.86	199.42	195.94
	23168R	173.46	167.73	173.53	167.66	173.46	167.72
	23169L	224.34	222.14	224.83	222.18	222.96	222.12
	23169R	174.79	167.66	177.68	168.10	173.17	167.86
	24170L	157.53	155.24	157.82	155.10	157.55	155.24
	24170R	143.97	139.89	144.10	139.97	143.98	139.90
	24175L	154.39	153.71	154.40	153.43	154.39	153.73
	24175R	189.36	187.33	189.56	187.34	189.64	187.49
	Average ± SD	**190.89 ± 47.57**	**187.21 ± 47.88**	**191.20 ± 47.58**	**187.11 ± 47.85**	**190.90 ± 47.99**	**187.19 ± 47.89**

No significant differences between average values were found.

Table 3.6: Volumetric bone mineral density (vBMD) in the **articular surface of the humerus head of cadaver specimens** derived using two dual-energy CT reconstruction kernels with three energy pair combinations using the $\boldsymbol{K_2HPO_4}$ calibration phantom.

	Model	40/90 keV		90/140 keV		40/140 keV	
		BONE	STD	BONE	STD	BONE	STD
vBMD [mgK_2HPO_4/cc]	**23162L**	199.95	195.64	199.63	195.42	199.91	195.61
	23162R	179.38	177.12	179.12	176.88	179.34	177.09
	23163L	163.48	158.96	163.38	158.81	163.48	158.94
	23163R	143.85	137.67	143.75	137.27	143.82	137.62
	23167L	341.33	328.99	341.36	328.50	341.35	328.99
	23167R	209.86	205.67	209.47	205.20	209.99	205.44
	23168L	195.26	191.32	194.63	191.25	195.23	191.47
	23168R	168.21	162.01	167.86	161.80	168.18	161.98
	23169L	225.18	219.75	225.23	219.95	225.08	219.22
	23169R	175.43	167.74	172.98	169.05	175.08	168.44
	24170L	152.59	149.25	152.92	148.97	152.61	149.24
	24170R	138.95	138.06	138.70	137.88	138.90	138.04
	24175L	153.09	154.07	153.08	154.44	153.10	154.62
	24175R	190.87	190.27	191.20	189.98	190.44	189.79
	Average ± SD	**188.40 ± 50.86**	**184.04 ± 48.66**	**188.09 ± 50.92**	**183.96 ± 48.56**	**188.32 ± 50.87**	**184.04 ± 48.58**

No significant differences between average values were found.

3.2 Participants vBMD results

All participants were scanned using the HA calibration phantom. The baseline vBMD results showed trends consistent with those observed in cadaver specimens. In the diaphysis, vBMD values were highest when using the BONE reconstruction kernel and higher energy pair combinations (90/140 keV), while the anatomical neck consistently showed the lowest vBMD values (Table 3.7 and Table 3.8). Due to limitations in sample size, ANOVA was not performed on the mean vBMD values.

Table 3.7: Volumetric bone mineral density (vBMD) in the **humeral shaft diaphysis of participants** derived using two dual-energy CT reconstruction kernels with three energy pair combinations using the **HA** calibration phantom.

	ID	40/90 keV		90/140 keV		40/140 keV	
		BONE	STD	BONE	STD	BONE	STD
vBMD [mgHA/cc]	**Participant 0001**	529.73	549.11	628.16	588.35	544.90	552.94
	Participant 0002	559.83	569.60	624.69	583.69	554.41	571.08
	Participant 0003	487.16	445.68	589.09	502.53	493.67	449.19

Table 3.8: Volumetric bone mineral density (vBMD) in the **anatomical neck of the humerus of participants** derived using two dual-energy CT reconstruction kernels with three energy pair combinations using the **HA** calibration phantom.

vBMD [mgHA/cc]	ID	40/90 keV		90/140 keV		40/140 keV	
		BONE	STD	BONE	STD	BONE	STD
	Participant 0001	218.81	219.89	218.14	219.81	217.32	219.56
	Participant 0002	122.83	118.41	122.82	118.08	123.07	118.39
	Participant 0003	151.35	148.14	156.76	156.03	151.63	148.60

Table 3.9: Volumetric bone mineral density (vBMD) in the **articular surface of the humerus head of participants** derived using two dual-energy CT reconstruction kernels with three energy pair combinations using the **HA** calibration phantom.

vBMD [mgHA/cc]	ID	40/90 keV		90/140 keV		40/140 keV	
		BONE	STD	BONE	STD	BONE	STD
	Participant 0001	274.70	280.92	266.93	280.83	274.62	280.86
	Participant 0002	175.34	174.14	175.14	173.90	175.64	174.13
	Participant 0003	234.85	197.97	243.96	208.01	235.40	198.56

3.3 Participants follow-up vBMD results

Two of the three participants were scanned at six months follow up using the HA calibration phantom. As observed at baseline, vBMD values remained highest in the diaphysis and lowest in the anatomical neck (Table 3.10 and Table 3.11). Notably, one participant exhibited unusually high vBMD values in the diaphysis at follow-up (Table 3.10). Due to the limited sample size, ANOVA was not performed on the mean vBMD values.

Table 3.10: Volumetric bone mineral density (vBMD) at **6-month follow-up** in the **humeral shaft diaphysis of participants** derived using two dual-energy CT reconstruction kernels with three energy pair combinations using the **HA** calibration phantom.

vBMD [mgHA/cc]	**ID**	**40/90 keV**		**90/140 keV**		**40/140 keV**	
		BONE	**STD**	**BONE**	**STD**	**BONE**	**STD**
	Participant 0001	508.64	522.43	563.10	538.11	515.24	527.61
	Participant 0002	816.89	796.63	1102.55	931.00	832.86	804.61

Table 3.11: Volumetric bone mineral density (vBMD) at **6-month follow-up** in the **anatomical neck of the humerus of participants** derived using two dual-energy CT reconstruction kernels with three energy pair combinations using the **HA** calibration phantom.

vBMD [mgHA/cc]	**ID**	**40/90 keV**		**90/140 keV**		**40/140 keV**	
		BONE	**STD**	**BONE**	**STD**	**BONE**	**STD**
	Participant 0001	147.28	145.68	147.08	145.88	147.24	145.69
	Participant 0002	214.89	195.37	212.12	196.01	214.73	195.39

Table 3.12: Volumetric bone mineral density (vBMD) at **6-month follow-up** in the **articular surface of the humerus head of participants** derived using two dual-energy CT reconstruction kernels with three energy pair combinations using the **HA** calibration phantom.

vBMD [mgHA/cc]	**ID**	**40/90 keV**		**90/140 keV**		**40/140 keV**	
		BONE	**STD**	**BONE**	**STD**	**BONE**	**STD**
	Participant 0001	206.01	209.25	205.89	209.36	205.98	209.25
	Participant 0002	198.77	190.12	198.66	192.93	198.75	190.27

3.4 Cadaver specimens FEM results

FEM of the diaphysis revealed significant differences between all energy pair combinations for BONE kernel images ($p < 0.0038$) (Table 3.13). No such significant differences were found amongst energy pairs within the STD kernel (Table 3.13). Interaction effects

revealed significant differences between BONE 90/140 keV and all STD kernel energy combinations, as well as between BONE 40/90 keV and STD 40/140 keV pairs ($p < 0.001$) (Table 3.13). No significant differences were found in FEM results within the anatomical neck, although FEM values were notably lower than those obtained from the diaphysis (Table 3.14).

Table 3.13: Finite element modeled (FEM) stiffness in the **humeral shaft diaphysis of cadaver specimens** derived using two dual-energy CT reconstruction kernels with three energy combinations using the $\boldsymbol{K_2HPO_4}$ calibration phantom.

	Model	40/90 keV		90/140 keV		40/140 keV	
		BONE	**STD**	**BONE**	**STD**	**BONE**	**STD**
Stiffness [kN/mm]	**23162L**	190.96	205.00	263.31	219.65	201.73	201.60
	23162R	188.07	198.51	252.93	212.98	187.57	192.69
	23163L	207.97	227.90	287.96	250.79	214.39	226.22
	23163R	197.93	220.09	270.47	232.06	202.95	216.39
	23167L	257.67	265.70	306.85	271.69	262.16	264.95
	23167R	244.65	253.72	284.50	258.08	249.78	250.65
	23168L	124.03	115.59	152.16	115.90	127.50	115.16
	23168R	110.66	110.53	144.00	104.91	113.37	107.17
	23169L	145.31	125.10	163.31	125.63	143.71	129.55
	23169R	138.67	124.71	151.97	122.25	146.67	121.51
	24170L	140.60	117.45	159.05	123.60	143.37	124.14
	24170R	138.65	114.10	152.23	113.32	136.21	115.23
	24175L	214.05	211.34	260.05	213.42	223.20	211.13
	24175R	225.02	218.23	277.34	228.29	233.77	222.79
	Average ± SD	**180.30 ± 47.07^{a,b}**	**179.14 ± 57.77^{d,g}**	**223.30 ± 63.91^{a,c,d,e,f}**	**185.18 ± 63.02^{e,g}**	**184.74 ± 48.98^{b,c}**	**178.51 ± 56.74^{f}**

Average values sharing a common letter are significantly different using a two-way RM-ANOVA (a,c,d,e,f: $p < 0.05$; b: $p = 0.0038$; g: $p = 0.041$).

Table 3.14: Finite element modeled (FEM) stiffness in the **anatomical neck of the humerus of cadaver specimens** derived using two dual-energy CT reconstruction kernels with three energy combinations using the K_2HPO_4 calibration phantom.

	Model	40/90 keV		90/140 keV		40/140 keV	
		BONE	STD	BONE	STD	BONE	STD
Stiffness [kN/mm]	**23162L**	115.83	103.18	113.32	101.17	114.43	101.94
	23162R	114.70	100.47	112.17	97.62	113.32	99.12
	23163L	125.56	104.40	121.72	104.87	123.39	102.46
	23163R	116.20	96.80	119.00	93.76	117.92	93.66
	23167L	188.39	189.72	188.38	186.97	187.60	190.00
	23167R	190.16	190.60	187.80	189.60	192.66	187.32
	23168L	85.16	71.60	84.42	74.04	85.12	70.20
	23168R	72.08	59.25	71.75	58.50	68.99	57.14
	23169L	107.00	93.27	106.40	93.69	103.30	93.62
	23169R	100.10	83.29	99.44	83.74	96.45	82.83
	24170L	122.14	102.40	122.57	102.50	119.71	100.47
	24170R	118.78	103.75	116.17	100.51	117.08	102.94
	24175L	108.72	92.60	112.78	93.47	110.07	93.65
	24175R	134.65	125.56	133.79	127.02	133.08	126.85
	Average ± SD	**121.37 ± 32.92**	**108.35 ± 38.07**	**120.69 ± 32.63**	**107.68 ± 37.54**	**120.22 ± 33.82**	**107.30 ± 38.09**

No significant differences between average values were found.

3.5 Participants baseline FEM results

At baseline, participants displayed notably higher FEM values in the diaphysis compared to the anatomical neck (Table 3.15 and Table 3.16). The highest FEM values in the diaphysis were observed in participants scanned using the BONE kernel at the highest energy pair combination (90/140 keV) (Table 3.15). Due to sample size restrictions, ANOVA was not performed on the mean FEM values.

Table 3.15: Finite element modeled (FEM) stiffness in the **humeral shaft diaphysis of participants** derived using two dual-energy CT reconstruction kernels with three energy combinations using the **HA** calibration phantom.

	ID	40/90 keV		90/140 keV		40/140 keV	
		BONE	STD	BONE	STD	BONE	STD
Stiffness [kN/mm]	**Participant 0001**	295.14	316.22	360.56	334.67	301.64	310.60
	Participant 0002	207.08	217.09	249.36	225.31	209.85	207.88
	Participant 0003	224.86	211.80	286.35	257.84	231.44	213.44

Table 3.16: Finite element modeled (FEM) stiffness in the **anatomical neck of the humerus of participants** derived using two dual-energy CT reconstruction kernels with three energy combinations using the **HA** calibration phantom.

Stiffness [kN/mm]	**ID**	**40/90 keV**		**90/140 keV**		**40/140 keV**	
		BONE	**STD**	**BONE**	**STD**	**BONE**	**STD**
	Participant 0001	219.76	215.36	209.61	213.19	214.95	250.41
	Participant 0002	111.79	100.18	110.92	101.70	111.70	100.09
	Participant 0003	123.83	149.81	132.69	163.12	125.66	151.16

3.6 Participants follow-up FEM results

Follow-up FEM results showed a similar trend to baseline, with the highest values observed in the diaphysis when participants were scanned using the BONE kernel at the highest energy pair combination (90/140 keV) (Table 3.17). No observable patterns were found in FEM values within the anatomical neck region (Table 3.18). Due to the limited sample size, ANOVA was not conducted on the mean FEM values.

Table 3.17: Finite element modeled (FEM) stiffness at **six-months follow-up** in the **humeral shaft diaphysis of participants** derived using two dual-energy CT reconstruction kernels with three energy combinations using the **HA** calibration phantom.

Stiffness [kN/mm]	**ID**	**40/90 keV**		**90/140 keV**		**40/140 keV**	
		BONE	**STD**	**BONE**	**STD**	**BONE**	**STD**
	Participant 0001	235.97	233.15	263.07	238.69	241.86	252.74
	Participant 0002	320.48	331.45	462.70	398.70	327.49	334.30

Table 3.18: Finite element modeled (FEM) stiffness at **six-months follow-up** in the **anatomical neck of the humerus of participants** derived using two dual-energy CT reconstruction kernels with three energy combinations using the **HA** calibration phantom.

Stiffness [kN/mm]	**ID**	**40/90 keV**		**90/140 keV**		**40/140 keV**	
		BONE	**STD**	**BONE**	**STD**	**BONE**	**STD**
	Participant 0001	186.28	176.11	183.30	176.38	187.39	170.22
	Participant 0002	254.31	236.67	256.62	233.20	252.94	235.81

3.7 Regression parameters for vBMD vs. Stiffness

R-squared values comparing BONE and STD kernels for both vBMD and stiffness were consistently high (≥ 95), indicating strong correlations across all comparisons (Table 3.19). Significant differences in regression slopes were observed between BONE and STD kernels for both vBMD and stiffness across all energy pair combinations. Additionally, a significant difference in the intercept was found for stiffness between BONE and STD kernels at the 90/140 keV energy pair. Across energy pairs, vBMD explained between 69 % and 78 % of the variance in FEM stiffness. Significant differences in slope were found across all kernel types and energy combinations, with a notable difference in intercept observed within the BONE kernel at 40/90 keV only (Table 3.19).

Table 3.19: Regression parameters for vBMD and FEM-based stiffness from the proximal humerus models in cadaver specimens from two dual-energy CT reconstruction kernels with three energy combinations.

Parameters	Slope			Intercept			R^2		
	40/90 keV	90/140 keV	40/140 keV	40/90 keV	90/140 keV	40/140 keV	40/90 keV	90/140 keV	40/140 keV
vBMD vs. Stiffness BONE	**0.382**	**0.411**	**0.387**	**53.542**	56.027	52.593	0.692	0.701	0.697
vBMD vs. Stiffness STD	**0.448**	**0.459**	**0.435**	26.591	23.510	30.096	0.784	0.775	0.774
BONE vs. STD vBMD	**1.096**	**0.924**	**1.076**	-23.773	**-23.860**	-25.732	0.970	0.991	0.979
BONE vs. STD Stiffness	**1.198**	**0.982**	**1.140**	**-36.825**	**-34.055**	**-32.173**	0.953	0.992	0.969

Values are reported as x vs. y in y = mx + b; m = slope, b = intercept. Significant differences ($p < 0.05$) between slope and intercept determined using linear regression analysis are shown in bold.

3.8 K_2HPO_4 vs. HA Regression Plots

Regression plots comparing K_2HPO_4 and HA calibration phantoms were generated to enable the translation of measurements between the two phantom types. This step is crucial for comparing DECT data from cadaver studies, where both phantoms are used, to participant data which is solely based on the HA phantom. It also ensures consistency and comparability in results, minimizing potential bias introduced by the choice of calibration phantom. Separate regression plots were created for each energy pair combination and reconstruction kernel (BONE and STD) across all anatomical regions analyzed.

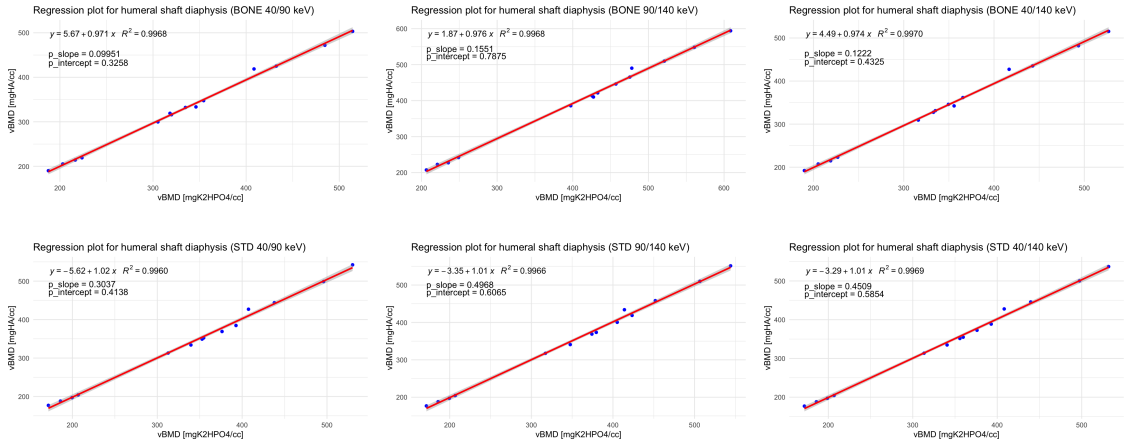


Figure 3.1: Linear regression of K_2HPO_4 vs. HA within each kernel and energy pair combination in the humeral shaft diaphysis.

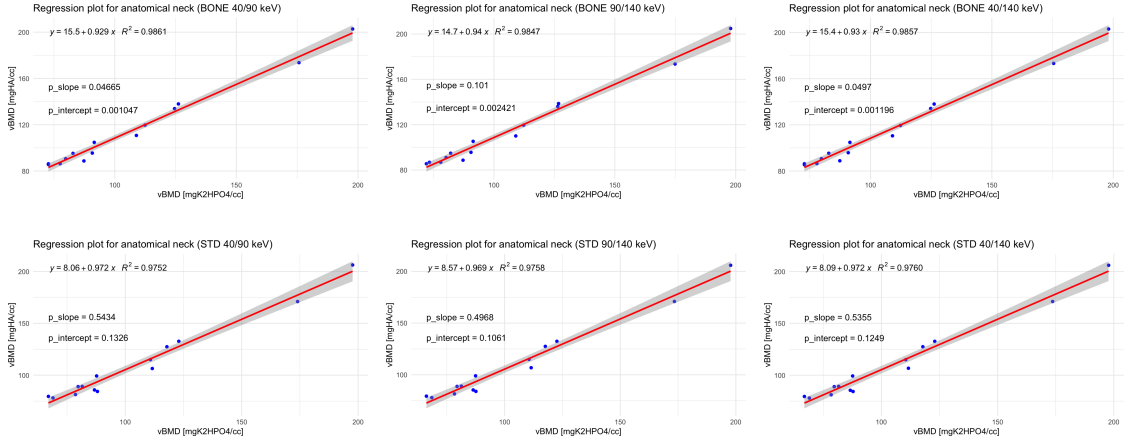


Figure 3.2: Linear regression of K_2HPO_4 vs. HA within each kernel and energy pair combination in the anatomical neck.

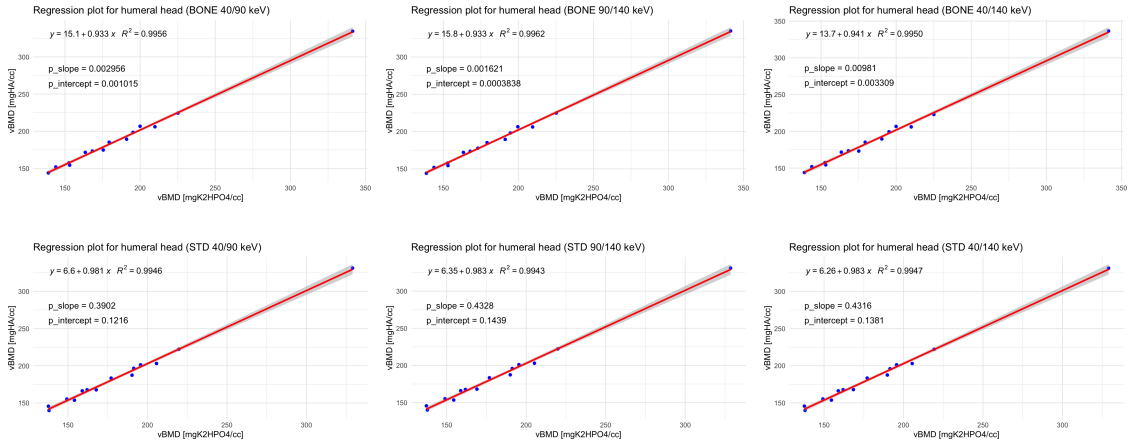


Figure 3.3: Linear regression of K_2HPO_4 vs. HA within each kernel and energy pair combination in the humeral head.

Chapter 4

Discussion

This study aimed to explore whether different high and low energy pair combinations used in DECT imaging could be used as an initial step toward developing image-based biomarkers for early detection of OA-related changes in the humerus. The highest vBMD and FEM-derived stiffness values were observed in the diaphysis, regardless of the kernel and energy pair combination, when compared to other regions of the proximal humerus. Specifically, at higher energy pairs (e.g. 90/140 keV), vBMD values in the BONE kernel appeared to be higher than those in the STD kernel within the diaphysis. Higher vBMD values in the diaphysis reflect its dense cortical bone composition. The use of the BONE kernel at higher energy pairs (e.g., 90/140 keV) enhances contrast and reduces noise, improving cortical bone measurements. In contrast, lower vBMD values in the anatomical neck, which is a mostly trabecular-rich region, highlight the challenges of measuring heterogeneous bone composition. Notably, the STD kernel exhibited higher slopes and lower intercepts compared to the BONE kernel which may reflect differences in how these kernels process image data.

Previous studies have established that reconstruction kernels affected vBMD and FEM outputs [54] and that DECT BONE kernel images typically had significantly higher vBMD compared to STD kernel images [47]. This increase in values can be attributed to the combined effects of kernel-specific image sharpening and improved energy-dependent material decomposition, both of which enhance image-derived bone density measurements [54]. The elevated vBMD also directly propagates to FEM-derived stiffness measurement calculations through the density-modulus relationship [47]. This relationship assumes that stiffer regions of bone correspond to areas of higher mineral density, which are enhanced in BONE kernel images due to their inherent image processing characteristics. The BONE kernel enhances edge definition and spatial resolution, which reduces partial volume effects

at bone-soft tissue interfaces and improves the delineation of cortical bone boundaries [54, 33]. This results in higher apparent densities in reconstructed images, particularly in regions of dense bone, and may also influence higher FEM-derived values [54]. Simultaneously, the use of high-energy pair combinations improves material decomposition by enhancing contrast between calcium and the surrounding soft tissues [54]. This reduces beam hardening effects, particularly in dense cortical bone, and improves the assignment of voxel-specific densities during reconstruction [47]. High-energy acquisitions are better at penetrating dense structures and provide more accurate attenuation measurements across the depth of the bone, leading to more reliable estimates of vBMD content and, by extension, the mechanical stiffness of the bone. The synergistic effect of the edge-enhancing properties of the BONE kernel and the improved spectral separation at 90/140 keV leads to elevated vBMD measurements [47]. This combination can also lead to artificially increased stiffness values in FEM-based simulations, especially in areas with high trabecular density or thick cortical shells, such as the diaphysis of the humerus. The higher FEM-derived stiffness values observed with BONE kernel reconstructions and high energy pair acquisitions are likely the result of a mix of increased bone-edge definition, improved attenuation measurement fidelity, and elevated vBMD values [47]. This combination also provides more accurate characterization of bone tissue properties and supports the use of optimized DECT protocols for biomechanical modeling in both research and clinical applications.

The novelty of this study lies in its combined analysis of vBMD and FEM-derived stiffness values using different reconstruction kernels with DECT energy pair combinations across different regions of the proximal humerus. By systematically comparing energy pair combinations and kernels, this study demonstrates that the 90/140 keV BONE configuration offers the most reliable and highest measurements, particularly in the diaphysis. This provides a practical guidance for developing imaging-based biomarkers for early post-traumatic risk of OA in the shoulder joint after first-time traumatic injury. While initial injuries in the shoulder, and subsequent OA-related changes, often occur at the articulating surfaces like the anatomical neck or humeral head, the diaphysis plays a vital biomechanical role in load transfer and long-term joint stability [28, 75]. Cortical bone quality in the diaphysis can influence joint mechanics and degeneration over time, which could serve as an early indicator of systemic bone changes post-injury, potentially before degeneration appears in the articular regions [28]. Currently, there are no established cutoff values for vBMD or FEM-derived stiffness in the proximal humerus that directly indicate early osteoarthritis risk following traumatic shoulder injury [28]. However, existing literature offers related thresholds and risk indicators that can inform clinical interpretation [28]. Low bone mineral density and reduced cortical bone thickness have been consistently identified as risk factors for poor outcomes following proximal humerus fractures, including secondary

OA [75]. In particular, a cortical bone thickness (CBT) of 4.52 mm, confirmed by MRI, has been shown to strongly correlate with low bone mineral density [28, 75]. Additional studies propose that CBT thresholds between 4 mm and 6 mm can serve as predictive markers for conditions such as osteoporosis, with measurements below these values suggesting compromised bone quality [28]. The results of this study consistently showed higher sensitivity and lower variance in the diaphysis when images were generated using the BONE kernel, allowing the detection of significant differences across scanning configurations, which were not evident in more trabecular-rich regions. In contrast, STD kernel values showed greater variance and weaker discriminatory power across energy pairs. These directional effects suggest that the imaging protocols used influence quantitative bone metrics and should be carefully selected for clinical imaging workflows targeting early OA detection. Overall, the BONE 90/140 keV configuration should be prioritized because it consistently produced the highest vBMD and FEM-derived stiffness values in both cadaveric and participant scans, particularly in the diaphysis. This configuration benefits from higher photon energy, which reduces image noise and beam-hardening artifacts, and the BONE kernel, which enhances edge definition and density contrast. These improvements translate into more accurate and reliable quantification of bone quality, especially in high-density cortical structures.

4.1 Limitations

As this study involved scanning the bilateral shoulders of each donor sample, one of the main concerns was whether there would be any problems of independence as the left and right shoulder originate from the same cadaver specimen. However, there are reasons as to why these measurements taken from each shoulder can be considered as separate observations. Although the shoulders are paired, they can undergo varying levels of mechanical stress, loading, or disease progression [6, 81]. Shoulders may also have different usage patterns that lead to varying responses to stress and adaptation [81, 51]. For example, predominantly using one arm for physical tasks, exercises, or injuries can lead to asymmetrical bone changes between shoulders and make them less correlated. As such, the bone changes in one shoulder might not directly influence or predict the changes in the other and can be considered as independent observations.

The choice of material decomposition method and the type of reconstruction kernel applied can significantly influence the results of vBMD and FEM stiffness. Research has shown that DECT-derived vBMD values can vary by up to 4.1 mgK_2HPO_4/cc between STD and BONE kernel images, with even greater differences in FEM stiffness results [47]. These discrepancies can arise because reconstruction kernels affect the spatial resolution

and noise levels in DECT images, and these effects cannot be fully corrected by calibration phantoms [47]. For example, the BONE kernel enhances high-frequency details in DECT images, leading to systematically higher vBMD and stiffness values [47]. Additionally, DECT scans are susceptible to noise amplification, especially in low-contrast regions, and artifacts such as photon starvation or metal implants that may not have been accounted for can further degrade imaging accuracy [66].

Moreover, FEM stiffness is influenced by the density-modulus relationship used which is often derived from non-shoulder sites (e.g., femur or spine) and can potentially leading to errors when applied to shoulder-specific models [46]. These relationships can either overestimate or underestimate stiffness values [46]. Future studies should determine the sensitivity to density-modulus relationships and develop anatomic location and vBMD input specific density-modulus relationships [47]. The exponential nature of density-modulus relationships can have large effects on vBMD inaccuracies which result in introducing errors in FEM measures [84, 47].

4.2 Conclusion

This study underscores the utility of DECT imaging in assessing regional variations in bone mineral density and mechanical stiffness in the proximal humerus. The findings demonstrate that different energy pair combinations and reconstruction kernels can influence vBMD and FEM measurements, highlighting the importance of protocol optimization for accurate bone assessment. While this study has provided meaningful insights, there are several directions for future research. Increasing the sample size in participant studies will enhance the statistical power to detect subtle differences in vBMD and FEM measurements across energy pair combinations. Longitudinal studies are needed to evaluate the ability of DECT to track OA-related changes over time and to determine the predictive validity of vBMD and FEM measurements for OA progression. Future studies could also explore the use of higher resolution imaging technologies, such as microCT, to extract additional information from DECT images and improve the accuracy of OA detection. In addition to vBMD and stiffness measurements, bone marrow lesions represent another potentially valuable measure for early OA detection. Although DECT is able to detect and characterize bone marrow abnormalities within the knee [25] and can be leveraged to identify early signs of OA-related changes in the bone marrow, validation studies against MRI would be required in the future to understand the impact and diagnostic value of DECT-detected BMLs in the context of shoulder OA.

The novel DECT imaging techniques can be used to monitor joint changes that may

lead to OA initiation and progression in all joints, providing a new paradigm in diagnostic patient care. Improved understanding of relationships between shoulder injury and early OA characteristics will improve therapeutic outcomes and assist in screening those at risk of OA development. Development of patient-specific image-based computational models will further advance our understanding of not only the biomechanical but also the image-based features of shoulder OA. Combined with clinical outcomes and longer-term follow-up of the participants in this study may allow for combined image-based, biomechanical, and clinical biomarkers that are predictive of those at highest risk for developing OA.

References

[1] Sejla Abdic, Nikolas K. Knowles, Gilles Walch, James A. Johnson, and George S. Athwal. Type e2 glenoid bone loss orientation and management with augmented implants. *Journal of Shoulder and Elbow Surgery*, 29(7):1460–1469, July 2020.

[2] Hatim Alabsi, Saleh Alreshoodi, Eugene Low, Nadia Sultan, Nicolas Murray, Paul Mallinson, Peter L. Munk, and Hugue A. Ouellette. Advancements in dual-energy ct applications for musculoskeletal imaging. *Current Radiology Reports*, 5(11):58, November 2017.

[3] Elizabeth M Badley, Jessica M Wilfong, Shatabdy Zahid, and Anthony V Perruccio. *Special Report: The Burden of Osteoarthritis in Canada*. 2021.

[4] Francis I. Baffour and Katrina N. Glazebrook. Dual-energy ct of musculoskeletal trauma. *Seminars in Roentgenology*, 56(1):106–114, January 2021.

[5] Julie C. Baker-LePain and Nancy E. Lane. Role of bone architecture and anatomy in osteoarthritis. *Bone*, 51(2):197–203, August 2012.

[6] Michael J. Bey, Roger Zauel, Stephanie K. Brock, and Scott Tashman. Validation of a new model-based tracking technique for measuring three-dimensional, in vivo glenohumeral joint kinematics. *Journal of Biomechanical Engineering*, 128(4):604–609, August 2006.

[7] Ann-Sofi Björkman, Seppo K Koskinen, Maria Lindblom, and Anders Persson. Diagnostic accuracy of dual-energy ct for detection of bone marrow lesions in the subacutely injured knee with mri as reference method. *Acta Radiologica*, 61(6):749–759, June 2020.

[8] Claire Bombardier, Gillian Hawker, and James G Wright. The impact of arthritis in canada: Today and over the next 30 years, 2001.

[9] Christian Booz, Jochen Noeske, Moritz H. Albrecht, Lukas Lenga, Simon S. Martin, Ibrahim Yel, Nicole A. Huizinga, Thomas J. Vogl, and Julian L. Wichmann. Diagnostic accuracy of quantitative dual-energy ct-based bone mineral density assessment in comparison to hounsfield unit measurements using dual x-ray absorptiometry as standard of reference. *European Journal of Radiology*, 132:109321, November 2020.

[10] Ana P. Borges, Célia Antunes, and Luís Curvo-Semedo. Pros and cons of dual-energy ct systems: "one does not fit all". *Tomography*, 9(1):195–216, 2023.

[11] Andrew M. Briggs, Jeremy Shiffman, Yusra Ribhi Shawar, Kristina Åkesson, Nuzhat Ali, and Anthony D. Woolf. Global health policy in the 21st century: Challenges and opportunities to arrest the global disability burden from musculoskeletal health conditions. *Best Practice & Research Clinical Rheumatology*, 34(5):101549, October 2020.

[12] Marina Carotti, Fausto Salaffi, Giacomo Beci, and Andrea Giovagnoni. The application of dual-energy computed tomography in the diagnosis of musculoskeletal disorders: a review of current concepts and applications. *La radiologia medica*, 124(11):1175–1183, November 2019.

[13] Marco Cavallaro, Tommaso D'Angelo, Moritz H. Albrecht, Ibrahim Yel, Simon S. Martin, Julian L. Wichmann, Lukas Lenga, Silvio Mazziotti, Alfredo Blandino, Giorgio Ascenti, Marcello Longo, Thomas J. Vogl, and Christian Booz. Comprehensive comparison of dual-energy computed tomography and magnetic resonance imaging for the assessment of bone marrow edema and fracture lines in acute vertebral fractures. *European Radiology*, 32(1):561–571, January 2022.

[14] Kevin Chan, Nikolas K. Knowles, Jean Chaoui, Louis M. Ferreira, Gilles Walch, and George S. Athwal. Is the walch b3 glenoid significantly worse than the b2? *Shoulder & Elbow*, 10(4):256–261, October 2018.

[15] Kevin Chan, Nikolas K. Knowles, Jean Chaoui, Marc-Olivier Gauci, Louis M. Ferreira, Gilles Walch, and George S. Athwal. Characterization of the walch b3 glenoid in primary osteoarthritis. *Journal of Shoulder and Elbow Surgery*, 26(5):909–914, May 2017.

[16] Lou-Ren Chang, Prashanth Anand, and Matthew A Varacallo. Anatomy, shoulder and upper limb, glenohumeral joint., August 2023.

[17] Xiaozhao Chen, Jinfeng Huang, Wei Zhang, Ruoran Li, and Yan Kang. Liquid phantom-based measurement of jaw bone density using cbct. *Journal of Mechanics in Medicine and Biology*, 22(09):2240061, November 2022.

[18] Gaurav Cheraya, Salil Sharma, and Avneesh Chhabra. Dual energy ct in musculoskeletal applications beyond crystal imaging: bone marrow maps and metal artifact reduction. *Skeletal Radiology*, 51(8):1521–1534, August 2022.

[19] Claudio Chillemi and Vincenzo Franceschini. Shoulder osteoarthritis. *Arthritis*, 2013:1–7, January 2013.

[20] Ismael Coifman, Ulrich H. Brunner, and Markus Scheibel. Dislocation arthropathy of the shoulder. *Journal of Clinical Medicine*, 11(7):2019, April 2022.

[21] Physics Department of Douglas College and Karine Hamm. 2.2.4 anatomy of selected synovial joints, Aug 2020.

[22] Matías Costa-Paz, D.Luis Muscolo, Miguel Ayerza, Arturo Makino, and Luis Aponte-Tinao. Magnetic resonance imaging follow-up study of bone bruises associated with anterior cruciate ligament ruptures. *Arthroscopy: The Journal of Arthroscopic & Related Surgery*, 17(5):445–449, May 2001.

[23] Eric Da Silva, Brian Kirkham, Darrick V. Heyd, and Ana Pejović-Milić. Pure hydroxyapatite phantoms for the calibration of in vivo x-ray fluorescence systems of bone lead and strontium quantification. *Analytical Chemistry*, 85(19):9189–9195, October 2013.

[24] Chantal M. J. De Bakker, Tushar Peedikayil, Richard E. A. Walker, Nathan J. Neeteson, Sarah L. Manske, and Steven K. Boyd. Diagnostic accuracy of a dual-energy computed tomography-based post-processing method for imaging bone marrow edema following an acute ligamentous knee injury. *Skeletal Radiology*, 51(9):1817–1827, September 2022.

[25] Chantal M.J. De Bakker, Nikolas K. Knowles, Richard E.A. Walker, Sarah L. Manske, and Steven K. Boyd. Independent changes in bone mineralized and marrow soft tissues following acute knee injury require dual-energy or high-resolution computed tomography for accurate assessment of bone mineral density and stiffness. *Journal of the Mechanical Behavior of Biomedical Materials*, 127:105091, March 2022.

[26] Chantal M.J. De Bakker, Richard E.A. Walker, Bryce A. Besler, Justin J. Tse, Sarah L. Manske, C. Ryan Martin, Stephen J. French, Andrew E. Dodd, and Steven K.

Boyd. A quantitative assessment of dual energy computed tomography-based material decomposition for imaging bone marrow edema associated with acute knee injury. *Medical Physics*, 48(4):1792–1803, April 2021.

[27] Sebastian Eberle, Michael Göttlinger, and Peter Augat. Individual density–elasticity relationships improve accuracy of subject-specific finite element models of human femurs. *Journal of Biomechanics*, 46(13):2152–2157, 2013.

[28] Sevde Nur Emir and Safiye Sanem Dereli Bulut. The role of humerus cortical thickness in predicting osteoporosis in mr imaging. *Shoulder & Elbow*, page 17585732241279090, September 2024.

[29] Andriy Fedorov, Reinhard Beichel, Jayashree Kalpathy-Cramer, Julien Finet, Jean-Christophe Fillion-Robin, Sonia Pujol, Christian Bauer, Dominique Jennings, Fiona Fennessy, Milan Sonka, John Buatti, Stephen Aylward, James V. Miller, Steve Pieper, and Ron Kikinis. 3d slicer as an image computing platform for the quantitative imaging network. *Magnetic Resonance Imaging*, 30(9):1323–1341, 2012.

[30] Giovanni Foti, William Mantovani, Niccolò Faccioli, Giacomo Crivellari, Luigi Romano, Claudio Zorzi, and Giovanni Carbognin. Identification of bone marrow edema of the knee: diagnostic accuracy of dual-energy ct in comparison with mri. *La radiologia medica*, 126(3):405–413, March 2021.

[31] Mihaela Gamala, Johannes W G Jacobs, and Jaap M Van Laar. The diagnostic performance of dual energy ct for diagnosing gout: a systematic literature review and meta-analysis. *Rheumatology*, 58(12):2117–2121, December 2019.

[32] Moges Gashaw, Fantu Mamo Aragaw, Ashenafi Zemed, Mastewal Endalew, Nuhamin Tesfa Tsega, Melaku Hunie Asratie, and Daniel Gashaneh Belay. Distal and/or proximal joint stiffness among post-fracture patients treated in university of gondar comprehensive specialized hospital, gondar, ethiopia. *Orthopedic Research and Reviews*, Volume 14:157–167, May 2022.

[33] Hugo Giambini, Dan Dragomir-Daescu, Paul M. Huddleston, Jon J. Camp, Kai-Nan An, and Ahmad Nassr. The effect of quantitative computed tomography acquisition protocols on bone mineral density estimation. *Journal of Biomechanical Engineering*, 137(11):114502, November 2015.

[34] Claus-C. Glüer, Ulrich J. Reiser, Craig A. Davis, Brian K. Rutt, and Harry K. Genant. Vertebral mineral determination by quantitative computed tomography (qct): Accu-

racy of single and dual energy measurements. *Journal of Computer Assisted Tomography*, 12(2):242–258, March 1988.

[35] Hyun Woo Goo and Jin Mo Goo. Dual-energy ct: New horizon in medical imaging. *Korean Journal of Radiology*, 18(4):555, 2017.

[36] Filippo Del Grande, Sahar J Farahani, John A Carrino, and Avneesh Chhabra. Bone marrow lesions: A systematic diagnostic approach. *Indian Journal of Radiology and Imaging*, 24(03):279–287, August 2014.

[37] Henry Gray. *Gray's anatomy*. Elsevier, 2021.

[38] Po-Chieh Hsu, Dmytro Luzhbin, Tia-Yu Shih, and Jay Wu. Diagnosis of osteoporosis by quantifying volumetric bone mineral density of lumbar vertebrae using abdominal ct images and two-compartment model. *Healthcare*, 11(4), 2023.

[39] Thomas Ibounig, Thomas Simons, Antti Launonen, and Mika Paavola. Glenohumeral osteoarthritis: an overview of etiology and diagnostics. *Scandinavian Journal of Surgery*, 110(3):441–451, September 2021.

[40] Xiuling Ji and Hongyu Zhang. Current strategies for the treatment of early stage osteoarthritis. *Frontiers in Mechanical Engineering*, 5, 2019.

[41] Nikolas K. Knowles, George S. Athwal, Jay D. Keener, and Louis M. Ferreira. Regional bone density variations in osteoarthritic glenoids: a comparison of symmetric to asymmetric (type b2) erosion patterns. *Journal of Shoulder and Elbow Surgery*, 24(3):425–432, March 2015.

[42] Nikolas K. Knowles, Michael J. Carroll, Jay D. Keener, Louis M. Ferreira, and George S. Athwal. A comparison of normal and osteoarthritic humeral head size and morphology. *Journal of Shoulder and Elbow Surgery*, 25(3):502–509, March 2016.

[43] Nikolas K. Knowles, Louis M. Ferreira, and George S. Athwal. The arthritic glenoid: anatomy and arthroplasty designs. *Current Reviews in Musculoskeletal Medicine*, 9(1):23–29, March 2016.

[44] Nikolas K. Knowles, Louis M. Ferreira, and George S. Athwal. Premorbid retroversion is significantly greater in type b2 glenoids. *Journal of Shoulder and Elbow Surgery*, 25(7):1064–1068, July 2016.

[45] Nikolas K. Knowles, Jay D. Keener, Louis M. Ferreira, and George S. Athwal. Quantification of the position, orientation, and surface area of bone loss in type b2 glenoids. *Journal of Shoulder and Elbow Surgery*, 24(4):503–510, April 2015.

[46] Nikolas K. Knowles, G.Daniel G. Langohr, Mohammadreza Faieghi, Andrew J. Nelson, and Louis M. Ferreira. A comparison of density–modulus relationships used in finite element modeling of the shoulder. *Medical Engineering & Physics*, 66:40–46, April 2019.

[47] Nikolas K. Knowles, Sarah Quayyum, Jonathan Ying, Chloe Stiles, and Daniel Beshay. Image-based finite element model stiffness and vbmd by single and dual energy ct reconstruction kernel. *Journal of Biomechanics*, 177:112426, December 2024.

[48] Jacek A. Kopec, Allison J. Heath, Eric C. Sayre, Jolanda Cibere, Linda C. Li, Carlo A. Marra, Ran R. Liu, and John M. Esdaile. Prevalence of joint-specific osteoarthritis and joint pain in british columbia, canada. *Rheumatology International*, 42(9):1623–1628, September 2022.

[49] Andres Kroker, Bryce A. Besler, Jennifer L. Bhatla, Mariya Shtil, Peter Salat, Nicholas Mohtadi, Richard E. Walker, Sarah L. Manske, and Steven K. Boyd. Longitudinal effects of acute anterior cruciate ligament tears on peri-articular bone in human knees within the first year of injury. *Journal of Orthopaedic Research*, 37(11):2325–2336, November 2019.

[50] Bradley M. Kruckeberg, Devin P. Leland, Christopher D. Bernard, Aaron J. Krych, Diane L. Dahm, Joaquin Sanchez-Sotelo, and Christopher L. Camp. Incidence of and risk factors for glenohumeral osteoarthritis after anterior shoulder instability: A us population–based study with average 15-year follow-up. *Orthopaedic Journal of Sports Medicine*, 8(11):232596712096251, November 2020.

[51] Simon Sw Li and Daniel Hk Chow. Effects of asymmetric loading on lateral spinal curvature in young adults with scoliosis: A preliminary study. *Prosthetics & Orthotics International*, 42(5):554–562, October 2018.

[52] Ying Liang Low and Eric Finkelstein. Cost-effective analysis of dual-energy computed tomography for the diagnosis of occult hip fractures among older adults. *Value in Health*, 24(12):1754–1762, December 2021.

[53] Matthew D. Mahaffy, Nikolas K. Knowles, Carolyn Berkmortel, Sejla Abdic, Gilles Walch, James A. Johnson, and George S. Athwal. Density distribution of the

type e2 glenoid in cuff tear arthropathy. *Journal of Shoulder and Elbow Surgery*, 29(1):167–174, January 2020.

[54] Andrew S. Michalski, W. Brent Edwards, and Steven K. Boyd. The influence of reconstruction kernel on bone mineral and strength estimates using quantitative computed tomography and finite element analysis. *Journal of Clinical Densitometry*, 22(2):219–228, April 2019.

[55] Peter J Millett, Reuben Gobezie, and Robert E Boykin. Shoulder osteoarthritis: Diagnosis and management. *American Family Physician*, 78(5):605–611, September 2008.

[56] Mohammed A Miniato, Prashanth Anand, and Matthew A Varacallo. Anatomy, shoulder and upper limb, shoulder., July 2023.

[57] Atousa Montaseri, Mohammadreza Alinaghizadeh, and Seied Rabi Mahdavi. Physical properties of ethyl methacrylate as a bolus in radiotherapy. *Iranian Journal of Medical Physics*, 9(2), June 2012.

[58] Ara Nazarian, Brian D. Snyder, David Zurakowski, and Ralph Müller. Quantitative micro-computed tomography: A non-invasive method to assess equivalent bone mineral density. *Bone*, 43(2):302–311, August 2008.

[59] E.H.G. Oei, J. Hirvasniemi, S. Klein, R.A. Van Der Heijden, S.M. Eijgenraam, D. Schiphof, S.M.A. Bierma-Zeinstra, and J. Runhaar. The 15th international workshop on osteoarthritis imaging; "open up: The multifaceted nature of oa imaging". *Osteoarthritis Imaging*, 2(1):100009, March 2022.

[60] E.H.G. Oei, J. Hirvasniemi, T.A. Van Zadelhoff, and R.A. Van Der Heijden. Osteoarthritis year in review 2021: imaging. *Osteoarthritis and Cartilage*, 30(2):226–236, February 2022.

[61] Public Health Agency of Canada. *Osteoarthritis in Canada*. 2020.

[62] Jorn Op Den Buijs and Dan Dragomir-Daescu. Validated finite element models of the proximal femur using two-dimensional projected geometry and bone density. *Computer Methods and Programs in Biomedicine*, 104(2):168–174, November 2011.

[63] Junhan Pan, Luyou Yan, Hui Gao, Yewen He, Zeya Zhong, Ping Li, Yaxi Zhang, Ying Guo, Liangying Liao, Shuwei Zhou, and Kun Zhang. Fast kilovoltage (kv)-switching

dual-energy computed tomography hydroxyapatite (hap)-water decomposition technique for identifying bone marrow edema in vertebral compression fractures. *Quantitative Imaging in Medicine and Surgery*, 10(3):604–611, March 2020.

[64] Bhavik N. Patel, Artem T. Boltyenkov, Maria G. Martinez, Domenico Mastrodicasa, Daniele Marin, R. Brooke Jeffrey, Benjamin Chung, Pari Pandharipande, and Avinash Kambadakone. Cost-effectiveness of dual-energy ct versus multiphasic single-energy ct and mri for characterization of incidental indeterminate renal lesions. *Abdominal Radiology*, 45(6):1896–1906, June 2020.

[65] R. Paul, N. Knowles, J. Chaoui, M-O. Gauci, L. Ferreira, G. Walch, and G. S. Athwal. Characterization of the dysplastic walch type c glenoid. *The Bone & Joint Journal*, 100-B(8):1074–1079, August 2018.

[66] Michael Petrongolo and Lei Zhu. Noise suppression for dual-energy ct through entropy minimization. *IEEE Transactions on Medical Imaging*, 34(11):2286–2297, November 2015.

[67] Physics Labs. Wave optics - physics 20800 lab 3. *Physics Labs*, 2024. Accessed: April 2, 2025.

[68] Julia M. Poleschinski, Nele Eley, Dirk Enderlein, Martin Kramer, Michael Lierz, and Dominik Fischer. A novel dipotassium hydrogen phosphate phantom for calibrating computed tomographic bone density measurements in birds. *Journal of Avian Medicine and Surgery*, 36(1), May 2022.

[69] Kristin L. Popp, Kathryn E. Ackerman, Sara E. Rudolph, Fjola Johannesdottir, Julie M. Hughes, Adam S. Tenforde, Miriam A. Bredella, Chun Xu, Ginu Unnikrishnan, Jaques Reifman, and Mary L. Bouxsein. Changes in volumetric bone mineral density over 12 months after a tibial bone stress injury diagnosis: Implications for return to sports and military duty. *The American Journal of Sports Medicine*, 49(1):226–235, January 2021.

[70] Prabhakar Rajiah, Murali Sundaram, and Naveen Subhas. Dual-energy ct in musculoskeletal imaging: What is the role beyond gout? *American Journal of Roentgenology*, 213(3):493–505, September 2019.

[71] Sumit Raniga, Nikolas K. Knowles, Emily West, Louis M. Ferreira, and George S. Athwal. The walch type b humerus: glenoid retroversion is associated with torsional differences in the humerus. *Journal of Shoulder and Elbow Surgery*, 28(9):1801–1808, September 2019.

[72] Qiuping Ren, Deqiu Tang, Zhiyuan Xiong, Heng Zhao, and Shuixing Zhang. Traumatic bone marrow lesions in dual-energy computed tomography. *Insights into Imaging*, 13(1):174, October 2022.

[73] Fausto Salaffi, Marina Carotti, and Antonio Barile. Musculoskeletal imaging of the inflammatory and degenerative joints: current status and perspectives. *La radiologia medica*, 124(11):1067–1070, November 2019.

[74] Bryan M. Saltzman, Eric J. Cotter, Jeffrey P. Stephens, Gregory L. Cvetanovich, Brett Madden, Kevin Wang, Adam B. Yanke, and Brian J. Cole. Preoperative tibial subchondral bone marrow lesion patterns and associations with outcomes after isolated meniscus allograft transplantation. *The American Journal of Sports Medicine*, 46(5):1175–1184, April 2018.

[75] Florian Schmidutz, Shuang G. Yan, Christoph Schopf, Christoph Ihle, Marc-Daniel Ahrend, and Christoph M. Sprecher. Cortical bone thickness predicts the quantitative bone mineral density of the proximal humerus. *Archives of Osteoporosis*, 16(1):33, December 2021.

[76] Jad G. Sfeir, Matthew T. Drake, Elizabeth J. Atkinson, Sara J. Achenbach, Jon J. Camp, Amanda J. Tweed, Louise K. McCready, Lifeng Yu, Mark C. Adkins, Shreyasee Amin, and Sundeep Khosla. Evaluation of cross-sectional and longitudinal changes in volumetric bone mineral density in postmenopausal women using single- versus dual-energy quantitative computed tomography. *Bone*, 112:145–152, July 2018.

[77] Sharifah Zakiah Syed Sulaiman, Wei Miao Tan, Rozanaliza Radzi, Intan Nur Fatiha Shafie, Mokrish Ajat, Rozaihan Mansor, Suhaila Mohamed, Angela Min Hwei Ng, and Seng Fong Lau. Comparison of bone and articular cartilage changes in osteoarthritis: a micro-computed tomography and histological study of surgically and chemically induced osteoarthritic rabbit models. *Journal of Orthopaedic Surgery and Research*, 16(1):663, December 2021.

[78] Fulvia Taddei, Enrico Schileo, Benedikt Helgason, Luca Cristofolini, and Marco Viceconti. The material mapping strategy influences the accuracy of ct-based finite element models of bones: An evaluation against experimental measurements. *Medical Engineering & Physics*, 29(9):973–979, 2007.

[79] Aran Toshav. Economics of dual-energy ct: Workflow, costs, and benefits. *Seminars in Ultrasound, CT and MRI*, 43(4):352–354, August 2022.

[80] Karen L. Troy and W. Brent Edwards. Practical considerations for obtaining high quality quantitative computed tomography data of the skeletal system. *Bone*, 110:58–65, 2018.

[81] Joshua William Giles, Louis Miguel Ferreira, George Singh Athwal, and James Andrew Johnson. Development and performance evaluation of a multi-pid muscle loading driven in vitro active-motion shoulder simulator and application to assessing reverse total shoulder arthroplasty. *Journal of Biomechanical Engineering*, 136(12):121007, December 2014.

[82] Sarah C.P. Williams. Subchondral sclerosis? causes, symptoms, and treatment, September 2024. Accessed: 2025-03-19.

[83] Mitchell P. Wilson, Kevin Lui, Dorian Nobbee, Mohammad H. Murad, Prayash Katlariwala, and Gavin Low. Diagnostic accuracy of dual-energy ct for detecting bone marrow edema in patients with acute knee injuries: a systematic review and meta-analysis. *Skeletal Radiology*, 50(5):871–879, May 2021.

[84] C. Winsor, X. Li, M. Qasim, C.R. Henak, P.J. Pickhardt, H. Ploeg, and M. Viceconti. Evaluation of patient tissue selection methods for deriving equivalent density calibration for femoral bone quantitative ct analyses. *Bone*, 143:115759, February 2021.

[85] William D. Wong, Mohammed F. Mohammed, Savvas Nicolaou, Heiko Schmiedeskamp, Faisal Khosa, Nicolas Murray, and Francesco Macri. Impact of dual-energy ct in the emergency department: Increased radiologist confidence, reduced need for follow-up imaging, and projected cost benefit. *American Journal of Roentgenology*, 215(6):1528–1538, December 2020.

[86] Laura A. Wyatt and Michael Doherty. *Morphological aspects of pathology*, volume 1. Oxford University Press, November 2016.

[87] Luyou Yan, Zeya Zhong, Hui Gao, Yewen He, Ping Li, Hongrong Shen, Shuwei Zhou, Ying Guo, Liangying Liao, and Kun Zhang. Fast kilovoltage (kv)-switching dual-energy ct virtual noncalcium technique using different reconstruction kernels for identifying acute and chronic vertebral compression fractures. *Archives of Osteoporosis*, 16(1):85, June 2021.

[88] Paul A. Yushkevich, Joseph Piven, Heather Cody Hazlett, Rachel Gimpel Smith, Sean Ho, James C. Gee, and Guido Gerig. User-guided 3D active contour segmentation of

anatomical structures: Significantly improved efficiency and reliability. *Neuroimage*, 31(3):1116–1128, 2006.

[89] Shuwei Zhou, Suping Chen, Xu Zhu, Tian You, Ping Li, Hongrong Shen, Hui Gao, Yewen He, and Kun Zhang. Associations between paraspinal muscles fatty infiltration and lumbar vertebral bone mineral density – an investigation by fast kvp switching dual-energy ct and qct. *European Journal of Radiology Open*, 9:100447, 2022.

[90] Philippe K Zysset, Enrico Dall'Ara, Peter Varga, and Dieter H Pahr. Finite element analysis for prediction of bone strength. *BoneKEy Reports*, 2, August 2013.

APPENDIX

Appendix A

CT methods equation derivation

A.1 Volumetric bone mineral density (vBMD) calibration method

To extract vBMD values from the four regions of the proximal humerus, simulated DECT images were processed using a custom Python script based on methods by de Bakker et al. (2022) [25]. The script applies linear regression between low- and high-energy images to correlate the CT numbers of calibration phantom rods (40, 90, and 140 keV) with known densities, producing a single DECT image calibrated to $\mathbf{K_2HPO_4}$ or HA density. From this regression, calibration slopes (m_{low}^{HA}, m_{high}^{HA}) and intercepts (b_{low}^{HA}, b_{high}^{HA}) are derived for each energy level. Each voxel in the resulting image is assumed to contain HA, soft tissue, and fat, with the total CT number at each energy representing the sum of contributions from these components [25].

$$H^{low} = H_{HA}^{low*} f_{HA} + H_s^{low*} f_s + H_f^{low*} f_f$$

$$H^{high} = H_{HA}^{high*} f_{HA} + H_s^{high*} f_s + H_f^{high*} f_f$$

By applying the slope and intercept of the calibration phantom HA and assuming the conservation of volume and that the relationship between CT number and fat density is the same at both energies to improve stability [25], the equivalent density of HA (ρ_{HA}) is calculated for each voxel:

$$\rho_{HA} = \frac{(H^{high} - b_{HA}^{high}) - (H^{low} - b_{HA}^{low})}{m_{HA}^{high} - m_{HA}^{low}}$$